Deep hydration and lithospheric thinning at oceanic transform plate boundaries

Wang Zhikai [1], Singh Satish C. [1, *], Prigent Cecile [1], Gregory Emma P. M. [1], Marjanovic Milena [1]

[1] Université Paris Cité, Institut de Physique du Globe de Paris, CNRS, Paris, France

* Corresponding author ! Satish C. Singh, email address : singh@ipgp.fr

Abstract :

Transform faults accommodate the lateral motions between lithospheric plates, producing large earthquakes. Away from active transform boundaries, former oceanic transform faults also form the fracture zones that cover the ocean floor. However, the deep structure of these faults remains enigmatic. Here we present ultra-long offset seismic data from the Romanche transform fault in the equatorial Atlantic Ocean that indicates the presence of a low-velocity anomaly extending to similar to 60 km below sea level. We performed three-dimensional thermal modelling that suggests the anomaly is probably due to extensive serpentinization down to similar to 16 km, overlying a hydrated, shear mylonite zone down to 32 km. The water is considered to be sourced from seawater-derived fluids that infiltrate deep into the fault. Below 32 km is interpreted to be a low-temperature, water-induced melting zone that elevates the lithosphere-asthenosphere boundary, causing substantial thinning of the lithosphere at the transform fault. The presence of a thinned lithosphere at transform faults could explain observations of volcanism, thickened crust and intra-transform spreading centres at transform faults. It also suggests that migration and mixing of water-induced melt with the high-temperature melt may occur beneath the ridge axis.

Transform faults (TFs) were proposed by Tuzo Wilson in 1965 as a new class of plate boundaries that accommodate relative lateral motions of two adjacent lithospheric plates[1]. TFs are oceanic or continental, depending on the type of lithosphere they crosscut. Oceanic TFs offset two segments of mid-ocean ridges[1]. They comprise almost one-fifth of the total length of active global plate boundaries[2] (~48,000 km), but release sixteen times more seismic energy than the ~67,000 km-long spreading ridges[3]. Away from active transform boundaries, the oceanic TFs are preserved as fracture zones (FZs), which extend over entire ocean basins and form some of the most prominent and continuous features on the ocean floor. The crustal structure of a few oceanic TFs has been studied through geophysical surveys[4,5], but the properties and nature of the deep lithosphere and the

lithosphere-asthenosphere boundary (LAB) at TFs remain enigmatic. Here, we present the velocity structure of the lithosphere at the Romanche TF down to 60 km depth below sea level (bsl).

Our study area lies in the equatorial Atlantic Ocean across the Romanche TF (Fig. 1)[6], which offsets the slow-spreading Mid-Atlantic Ridge (~32 mm/yr full rate[7]) and has hosted several large earthquakes in the last 40 years[8]. The ~880 km-long[5] Romanche TF is among the largest active strike-slip plate boundaries on the Earth, comparable to its continental counterparts: the Dead Sea Fault (~1000 km long, slip rate of ~7.2 mm/yr), North Anatolian Fault (~1500 km long, slip rate of ~24 mm/yr) and San Andreas Fault (~1200 km long, slip rate of ~35 mm/yr)[9]. Therefore, investigating the structure beneath the Romanche TF is important not only for understanding of the mid-ocean ridge-transform fault systems, but also for the strike-slip plate boundaries.

Seismic velocity structure of the Romanche transform fault

We acquired a ~855 km-long seismic refraction profile using ocean-bottom seismographs (OBSs) (see Methods), crossing the Romanche TF (Fig. 1). The age contrast across the Romanche TF along the profile is ~32 Myr, with 8 Myr-old lithosphere to the south and 40 Myr-old lithosphere to the north[10]. In this region, the Romanche TF is characterized by a ~20 km-wide transform valley and a hanging basin on the northern flank. Previous studies have suggested that the region around the eastern ridge-transform intersection (RTI) of the Romanche TF is cold and displays an extremely thin crust[11]. However, recent seismic studies suggested that the crust is 5.5-6.5 km thick at the Romanche TF[5], and the LAB lies at ~72 km depth beneath the 40 Myr-old lithosphere north of the transform[12], arguing for the presence of a normal lithosphere in this region.

The mantle refraction arrivals (Pn) are observed to 250 km offsets for most OBSs, and six OBSs record Pn arrivals up to ~700 km offsets (Fig. 2 and Supplementary Figs. 1, 2). The nearly flat Pn arrivals on the recorded pressure data (Fig. 2, Extended Data Fig. 1 and Supplementary Fig. 2) suggest that the mean P-wave velocity in the ridge-parallel direction for the uppermost mantle along the seismic profile is consistent with those observed in other regions of the Mid-Atlantic Ocean (7.9-8.1 km/s)[13]. The travel time delays and weak amplitudes observed on several OBSs (Extended Data Fig. 1) for the rays entering the Romanche transform zone imply the possible presence of a low-velocity structure in the mantle below the transform valley.

To investigate the velocity structure of the lithosphere, we first perform two-dimensional ray-based travel time tomography[14] of the manually picked arrival times of the crustal refractions and the reflections from the Mohorovičić discontinuity (Moho) to constrain the crustal velocity and the depth of the Moho (see Methods). Then the mantle velocity is estimated by inverting the picked Pn arrival times using a similar tomography method (see Methods).

The tomographic result (Fig. 3a and Extended Data Fig. 2a) shows that the lithosphere at the Romanche transform zone is characterized by a deep-rooted low-velocity anomaly

(LVA), extending down to ~60 km depth bsl. Below the transform valley, the mantle velocity is ~7.37 km/s just below the Moho (Figs. 3a, b), which corresponds to an ~8% reduction relative to the surrounding mantle velocity (~7.85-8.0 km/s; Fig. 3a). The velocity reduction of the LVA decreases with depth to ~1% at 60 km depth. A Monte-Carlo-based uncertainty analysis indicates that the velocity variance at 60 km depth is ~0.4% (see Methods, Supplementary Fig. 3), supporting that the tomography method is sensitive enough to resolve the LVA. The tomographic vertical mantle velocity gradient within the LVA decreases rapidly from ~50 m/s/km just below the Moho to ~18 m/s/km at 16 km depth, then slowly to ~11 m/s/km at 32 km depth and remains nearly constant underneath with some slight undulations (Fig. 3b), revealing three distinct zones in depth range in contrast to the nearly constant velocity gradient (~5.6 m/s/km) in the mantle north of the Romanche TF (Fig. 3b).

The smearing studies using simulated models (see Methods, Extended Data Fig. 3) indicate that the LVA down to 60 km depth is not produced by the smearing effect of tomography and is therefore real. The resolution studies (see Methods, Supplementary Figs. 4, 5) demonstrate that the real decrease of mantle velocity within the LVA zone beneath the Romanche TF is likely to be much larger than that estimated by the tomographic method. This is because the ray-based tomography method used here can only provide a smooth velocity structure, under-estimating the velocity decrease significantly in the mantle beneath the Romanche TF. Furthermore, synthetic inversion tests demonstrate that the trends in the vertical mantle velocity gradient cannot be accounted for by smoothing effects of tomography (Supplementary Figs. 4h, 5h), and therefore they are a real representation of the velocity trend in the mantle beneath the TF. To quantify the real mantle velocity structure beneath the Romanche TF that would lead to the tomographically inverted LVA, we performed 60 inversion tests using simulated models. The synthetic models are designed by introducing LVA with varying percentage in velocity reductions at different depths and varying widths into a modified velocity model (Supplementary Fig. 6). Rays travelling in these simulated models are computed using the same source-receiver geometry as that of the Pn picks, and the modelled travel times are inverted employing the same tomography method used for the real OBS data. The resulting 60 inverted models are then compared with the tomographic velocity obtained using the real OBS dataset (see Methods, Supplementary Fig. 8 and Extended Data Table 1). Based on these comparisons, we found that the mantle velocity within the LVA increases from 6.89±0.12 km/s just below the Moho to 7.75±0.06 km/s at 60 km depth (Fig. 3b), with the width of the LVA varying from 34.1±3.9 km to 35.6±5.7 km, respectively (Extended Data Fig. 4a and Table 2). These estimates suggest that the real decrease in the LVA just below the Moho could be up to ~12.4% and 4.5% at 60 km depth. Based on these results and the changes in the vertical mantle velocity gradient (Fig. 3b), the lithospheric mantle beneath the Romanche TF can be divided into three zones: Zone 1 from the Moho down to 16 km depth, Zone 2 from 16 to 32 km depth and Zone 3 below 32 km down to 60 km depth.

Evidence for upper mantle hydration

To interpret the LVA at the Romanche TF, we perform three-dimensional thermal modelling with a temperature-dependent visco-plastic mantle rheology[15] to predict the thermal

structures of the Romanche TF and the adjacent normal lithosphere (see Methods, Fig. 4). Combined with the petrological constraints available from oceanic TFs[16–18], we interpret the LVA at the Romanche TF as being caused by hydration and/or deformation of the upper mantle, where hydration leads to mantle alterations (Zones 1 and 2) and hydrous mantle melting (Zone 3).

Brittle deformation induced by earthquakes on oceanic TFs could create and sustain high-permeability pathways for seawater-derived fluids to penetrate deep into the lithosphere. The resulting fluid-rock interactions and metamorphic reactions affect the compositional, structural and mechanical properties of TFs, and consequently, seismic velocities. Brittle deformation at oceanic TFs has been suggested to occur down to the ~600°C[8, 19]. However, recent petrological studies on peridotite mylonites dredged from some oceanic TFs indicate that seawater-derived fluids infiltrate down to depths corresponding to at least 850-875°C[16, 17], implying brittle deformation and mantle hydration at higher temperatures.

Petrological observations from natural samples collected on oceanic TFs show that fluid interaction with mantle rocks leads to metamorphic reactions whose nature is temperature dependent[16, 17] The fluid-rock interactions typically result in serpentinization of mantle peridotites below ~500-550°C[16, 17], triggering a significant decrease in seismic velocity[20]. At the Romanche TF, the predicted mantle temperature is 420°C at 16 km depth (Fig. 4). As this temperature is consistent with the upper stability limit of serpentine, we interpret Zone 1 to represent the serpentinized fault zone, delimited by the rapid change in vertical mantle velocity gradient at 16 km depth (Fig. 3b). In this case, 55±7% of mantle serpentinization would be required to account for the 12.4% decrease in velocity just below the Moho, decreasing to 25±5% at 16 km depth (see Methods, Extended Data Fig. 5). This depth is also coincident with the maximum focal depth of large earthquakes that have occurred in this region[8, 21], supporting our interpretation.

Above ~600°C, peridotites on oceanic TFs transition from a brittle to a semi-brittle behavior[16, 17]. Episodes of brittle deformation in the semi-brittle zone create transient-permeability pathways that drive the penetration of seawater-derived fluids and hydration reactions[16, 17], leading to the formation of hydrated and fine-grained mylonitic peridotites. The observed change in velocity gradient at 32 km depth (Fig. 3b) coincides with the 940°C isotherm (Fig. 4). Though it is slightly higher than the estimated maximum temperature (850-875°C) for the production of hydrated mylonites on oceanic TFs[16, 17], we interpret this depth as the base of the mylonite zone (Zone 2).

The hydration of peridotites could lead to the crystallization of hydrous minerals, such as chlorite and amphibole[16, 17] that exhibit lower seismic velocities than peridotites[22]. Assuming that the velocity anomaly in Zone 2 is mainly due to these hydration processes, the estimated fraction of hydrous minerals would decrease from 28±6% at 16 km depth to 10±7% at 32 km depth (see Methods, Extended Data Figs. 6a, b). The natural samples of peridotite mylonite dredged from oceanic TFs comprise of ~12.5% amphibole for mylonitization occurring at temperature >750°C and comprise ~16% chlorite and ~24% amphibole for mylonitization occurring at medium temperature (~500-750°C)[16]. Using the estimated fractions of hydrous minerals, our calculations suggest that 70±15% of the

mantle at 16 km depth and more than 24% of the mantle at 32 km depth would be mylonitic at the Romanche TF (Extended Data Figs. 6c, d). Although the change in velocity gradient at 16 km depth is rather sharp (Fig. 3b), there might be a transition zone where serpentine, chlorite, and amphibole co-exist as the predicted temperature at 16 km depth is lower than the stability of serpentine. A microseismic study from this region highlights a band of microseismicity between 21.3±1.4 km and 34.7±3.0 km depths bsl[23] (Fig. 3c and Supplementary Table 1), which is consistent with our interpretation of a zone made of hydrated mylonites at these depths.

Evidence for melt in the upper mantle

The LVA beneath 32 km depth at the Romanche TF, with a large and nearly constant vertical velocity gradient, cannot simply be explained by mantle anisotropy, temperature, and variations in composition. Mantle anisotropy could decrease the seismic velocity in the orthogonal direction of shear deformation, but it could not have produced a large and positive vertical mantle velocity gradient in this direction[24]. Furthermore, an excess temperature due to thermal diffusion cannot account for the low-velocity structure because the required temperature to reduce the velocity exceeds the solidus of mantle peridotite (see Methods, Supplementary Fig. 11). The presence of metasomatic peridotites could lower the mantle velocity; however, the plagioclase formation indicates that metasomatic reactions occur shallower than ~32 km depth bsl[11].

The LVA below 32 km depth could be explained by the presence of a small amount of melt in the mantle. Assuming the mantle beneath the Romanche TF starts melting at 32 km depth and using the effective medium theory[25], the estimated mantle velocities (Fig. 3b) would require 1.30±0.30% and 0.64±0.18% of melt at 32 km and 60 km depths, respectively, in the form of thin films with an aspect ratio of 50 (see Methods, Extended Data Fig. 7). Such thin films of melt could be produced by the localized shear deformations within the transform zone, and have been proposed to explain the low seismic velocity in the LAB beneath the equatorial Atlantic Ocean[12].

The solidus of a dry mantle at 32 km depth[26] is much higher than the predicted temperature at this depth within the transform zone (Extended Data Fig. 8a). At 60 km depth, the predicted temperature for TF is close to the solidus of a dry mantle (Extended Data Fig. 8b). This means the presence of volatiles, such as water and/or carbon dioxide, in the mantle is required to produce hydrous melt at low temperatures[26, 27] between 32 and 60 km depth. At the Romanche TF, the predicted temperature of 940°C at 32 km depth (Fig. 4) is slightly higher than the minimum temperature (~922°C[26]; Extended Data Fig. 8a) for melting a water-saturated mantle at this depth. Therefore, the water could be the main volatile driving hydrous mantle melting between 32 km and 60 km depth beneath the Romanche TF. To trigger hydrous mantle melting at these depths and the corresponding temperature-pressure conditions, the required water fraction would be 0.22 wt% at 32 km depth, decreasing to 0.0 wt% at 60 km depth (see Methods, Extended Data Fig. 8).

The hydrous mantle melting brings out the question of the source of water. One possibility is that water within the shallow lithosphere penetrates to 32 km depth, facilitated by the

seismicity-related fracturing within the brittle and semi-brittle lithosphere. Rheological modelling shows that the brittle-ductile transition occurs over 300-1000°C temperature range on oceanic TFs, arguing the seawater may percolate down to the base of the brittle-ductile transition zone[18]. Another possible source of water is the sub-lithospheric water-rich melt channel at the base of the oceanic lithosphere observed in the equatorial Atlantic region[12, 28]. The top boundary of this channel lies at ~72 km depth bsl north of the Romanche TF and corresponds to the 1260°C isotherm for the 40 Myr-old lithosphere[12]. If this boundary south of the Romanche TF also corresponds to 1260°C isotherm, it would lie at ~34 km depth bsl for the 8 Myr-old lithosphere (Fig. 4), which is slightly shallower than the depths of LAB obtained from Rayleigh wave tomography and receiver function modelling studies[29, 30]. The normal faulting observed in the eastern portion of the Romanche TF[23] and the gradual widening of the transform valley from the eastern RTI to our study area indicate some extensions in this region. Trans-tension along TF would uplift the LAB to a shallower depth, modifying the geotherm and consequently facilitating the hydrous mantle melting.

A schematic diagram summarising our interpretation is shown in Fig. 5. Our simulated tomographic study indicates a sharp boundary between the Romanche transform zone and the normal oceanic lithosphere on either side, but there could be a transition zone between the deep hydration zone beneath the TF and the normal oceanic lithosphere. Although we have used the uncertainties in the estimated widths of transition zones (Fig. 5), the real transition might be much more complex, especially for the water-induced melt zone. Secondly, the ray-based tomographic method cannot recover the low-velocity structure below ~34 km depth within the LAB south of Romanche TF as rays would avoid penetrating into the low-velocity LAB, possibly leading to slightly higher uncertainties in the velocity estimation. Thirdly, we have used the depth corresponding to the I260°C isotherm to represent the top of the LAB for the younger lithosphere south of the TF, but the real LAB might be slightly deeper[29, 30]. In any case, the top of the LAB would be at least 2 km shallower than the surrounding lithosphere, and the lithosphere would be thinner at the Romanche TF. If the 940°C isotherm constrains the depth of the lithosphere, then the lithosphere would be thin along the whole transform segment.

Effects of lithospheric thinning at oceanic transform faults

The presence of thin lithosphere would have a significant effect on the geodynamics of the ridge-transform system. It might account for some recent observations of thick magmatic crust at oceanic TF[5] and FZs[31, 32] in the equatorial Atlantic Ocean. Wide-spread volcanism is generally absent along oceanic TFs due to the cold edge effect[33]. However, the occurrences of volcanism along a few oceanic TFs[34] might be caused by the presence of a thinned lithosphere. The presence of thinned lithosphere would facilitate the occurrence of intra-transform spreading centres observed along large-offset TFs, such as the St Paul TF[35].

Recent numerical modelling studies indicate shallow and nearly flat isotherms at oceanic TFs[36, 37] (Supplementary Fig. 10). The presence of a thinned lithosphere and the melt underneath could lead to migration and mixing of the water-induced melt with the upwelling melt beneath the ridge axis. The petrology of basalts recovered along the equatorial MAR

shows increased water content in the melt northward approaching the Romanche TF[38], supporting the idea of melt migration and mixing. On the other hand, leaky transforms[39] might be manifestations of melt movement along thinned lithosphere. A thin lithosphere beneath oceanic TFs would also influence the evolution of oceanic FZs, and subsequently the evolution of oceanic lithosphere.

LVAs observed on major active continental TFs generally penetrate down to mid- or lower crust[40, 41]. At the central and eastern North Anatolian Fault, LVA is reported to merge into the asthenosphere[42], but it extends much shallower in the Marmara Sea[43]. This implies that continental TFs exhibit a complicated structure. Although the rheology and thermal structure of the lithosphere might be different, the mylonitization of the lithosphere due to localized shear deformation and partial melting at depth could be common features along oceanic and continental TFs.

Methods

Data acquisition

The ~855 km-long seismic profile was acquired in August-October 2018 during the ILAB-SPARC experiment conducted in the equatorial Atlantic Ocean aboard the French R/V 'Pourquoi Pas?'. Fifty four-component ocean bottom seismographs (OBSs) were deployed at ~14.2 km interval. The seismic source was composed of two sub-arrays with eight airguns on each array, producing a total volume of 81.77 litre. The airgun arrays were fired every 300 m at 10 m depth bsl. The maximum recording time for each shot is 130 s and the sampling rate is 4 ms. The pressure component of the seismic data recorded by hydrophones is used in this study.

Seismic data analysis and inversion

The travel times of Pg, PmP and Pn arrivals have been hand-picked on the seismic data after band-pass filtering (4-15 Hz for Pn arrivals and 4-20 Hz for Pg and PmP arrivals). The picking uncertainties are 30-50 ms for Pg arrivals, 50-70 ms for PmP arrivals and 45-100 ms for Pn arrivals, which are assigned based on the visibility of the seismic arrivals.

The seafloor depth and sediment thickness along the seismic profile are determined using the coincident bathymetry and seismic reflection data[5, 31]. The velocities of water and sediment are set to 1.5 km/s and 1.86 km/s in tomography[5, 31], respectively. The initial crustal velocity is constructed using a simplified one-dimensional velocity profile[5, 30] hanging from the basement. The initial crustal thickness is 5.5 km. The initial mantle velocity is extended from an one-dimensional velocity profile hanging from the Moho, where the velocity increases from 7.8 km/s with a gradient of 14.0 m/s/km for the top 20 km[24] and then gently increases with a gradient of 3.5 m/s/km to 90 km depth. The velocity model is discretized at 300 m horizontally and 60 m vertically.

We perform two-dimensional ray-based travel time tomography[14] to constrain the crustal and mantle velocity. The ray paths from sources to receivers and the corresponding travel times are calculated using the shortest path method[44]. The 'forward star' in the modelling using the shortest path method[44] comprise 15 nodes horizontally and 30 nodes vertically.

We first invert the Pg arrivals to constrain the velocity of the upper crust, followed by a joint inversion of Pg and PmP arrivals to constrain the crustal velocity and the Moho depth simultaneously. Then we fix the crustal structure and invert Pn arrivals only to constrain the mantle velocity. The strengths of first- and second-order smoothing penalties[14] are tested and selected in each iteration to avoid the introduction of artefacts. In the tomography of Pn arrivals, the imposed horizontal and vertical inversion correlation lengths are 15 km and 5 km, respectively. The final χ^2 value[14] is 1.6 for Pg and PmP arrivals and is 2.2 for Pn arrivals. The final RMS misfits[14] are 42 ms, 65 ms and 74 ms for Pg, PmP and Pn arrivals, respectively. We show the final tomographic model between 200 and 650 km profile distance in Fig. 3a and the tomographic model at full profile distance in Extended Data Fig. 2a. The plot of ray distributions shows the maximum sampling depth of rays is ~60 km bsl (Extended Data Fig. 2b).

We use a Monte-Carlo analysis method[45] to quantify the mantle velocity variance. A set of 100 linear-gradient mantle velocity models are created as initial models for tomographic inversion, where the mantle velocity gradients vary between 5 and 10 m/s/km and the velocity just below the Moho varies between 7.7 and 7.9 km/s. We then perform the same travel time tomography as described before to obtain 100 final models. We take the standard deviation of these final models as the mantle velocity variance (Supplementary Fig. 3). The velocity variances of the low velocity anomaly (LVA) are <0.03 km/s, which are much smaller than the velocity reductions (0.07-0.5 km/s) of the LVA in the tomographic model. At 60 km depth, the velocity variance within the LVA corresponds to ~0.4% velocity reduction relative to the surrounding mantle, which is much smaller than the ~1% velocity reduction in the tomographic result.

The vertical smearing effect on the tomographic result

We use synthetic tests to examine whether the observed LVA extending to ~60 km depth is real or is a result of vertical smearing effect[4] of tomography. The tests are performed using the initial model by inserting LVAs with different widths and vertical extents into the mantle beneath the Romanche TF. The maximum depths of the introduced LVAs are 30, 40 or 50 km, and their widths are 30 or 50 km. The inserted LVAs have a constant velocity reduction of 8%. We calculate the travel times for these simulated velocity models using the same source-receiver configuration as that used in the tomography of the OBS data and add some random travel time noise to mimic the picking uncertainty. Then we invert these synthetic travel time datasets using a similar two-dimensional tomography workflow (the same iteration process, smoothing strategy and parameters, initial model, and similar final χ^2) as that used in the tomography of the OBS dataset. The tomographic results (Extended Data Fig. 3) demonstrate that the amplitude of velocity reduction caused by the downward smearing effect is less than 0.5% below 35 km depth. This means the downward smearing effect cannot produce a 1% velocity reduction at 50-60 km depths, demonstrating that a LVA extending to ~60 km depth is required by the data and hence is real.

Resolution study for the width and velocity reduction

To evaluate the resolution of the tomographic model from the OBS data, we conduct two groups of tests using synthetic seismic datasets. LVAs with different widths and amplitudes

of velocity reduction are introduced into the initial model that was used in the tomography of the OBS data, extending from the Moho down to the base of the model. The width of the inserted LVA is constant in depth in each test. Similar to the smearing tests, synthetic travel time datasets are generated using these designed models and are inverted using a similar tomography workflow as that for the OBS data.

In the first group of tests, we fix the amplitude of velocity reduction within the introduced LVA to 8% and vary the width of the LVA from 25 km to 60 km (Supplementary Fig. 4). We take 8% of velocity reduction for the inserted LVAs because the maximum velocity reduction within the LVA obtained using the OBS data is ~8% (Fig. 3a). When the width of the introduced LVA is 25 km, the recovered velocity anomaly at the Moho is ~5%,with no recovery at 60 km depth (Supplementary Fig. 4a). As the width of the LVA increases, both the percentage and depth of the recovered velocity anomaly increase (Supplementary Figs. 4b-d). When the width of the LVA is 45-50 km, the 8% velocity reduction is recovered at the Moho, with ~1% recovered velocity anomaly at 50-60 km depths (Supplementary Figs. 4e, f), similar to the real LVA (Fig. 3a). Further increasing the width of the LVA to 60 km, ~2% of the anomaly at 50 km depth is recovered (Supplementary Fig. 4g).

In the second group of tests, we take a LVA with a constant width of 50 km as an example to study the influence of the amplitude of velocity reduction of the LVA on the tomographic result. We vary the percentage of velocity reduction within the LVA from 3% to 9% (Supplementary Fig. 5). For an LVA with less than 7% velocity anomaly, <1% of velocity anomaly is recovered at 60 km depth (Supplementary Fig. 5a-e). When the amplitude of velocity reduction of the LVA is 8%, ~8% velocity anomaly is recovered at the Moho, with ~1% recovered velocity anomaly at 60 km depth (Supplementary Fig. 5f). Further increasing the amplitude of the velocity reduction to 9%, the LVA can be better recovered (Supplementary Fig. 5g).

These tests suggest that the recovered 8% velocity anomaly just below the Moho at the Romanche TF using the OBS dataset requires a 50 km wide LVA with at least 8% velocity or larger velocity reduction if the width of the LVA is narrower than 50 km. In all the tests, the majority of the LVAs is not completely recovered, suggesting that the tomography method under-estimates the amplitude of the velocity anomaly significantly. The failure of constructing the sharp boundaries of the LVA using OBS data can possibly be attributed to the horizontal smoothing effect of tomographic inversion, which is clearly observed in all the tomographic results from the synthetic datasets (Supplementary Figs. 4, 5). Since the amplitude of the introduced velocity anomaly is kept constant for the whole column in each test, the recovered vertical mantle velocity gradient beneath the Romanche TF decreases smoothly with depth (Supplementary Figs. 4h, 5h), which is different from the inverted velocity gradient using the OBS data. This implies that the velocity reduction of the real LVA beneath the Romanche TF varies with depth.

LVA with changing velocity reduction with depth

Resolution tests demonstrate that the tomography method under-estimates the amplitude of the velocity anomaly significantly. To quantify the width and velocity reduction of the real LVA beneath the Romanche TF, we perform a series of tests following the

concepts of geophysical inversion. Firstly, we design a base mantle velocity model (model A, Supplementary Fig. 6) by removing the LVA from the tomographic velocity model from OBS data (Fig. 3a) and replacing it by interpolating mantle velocity of the normal lithosphere on both sides. We then introduce LVA with different widths and changing velocity reduction with depth into model A beneath the Romanche TF to create a suite of models. The depths of 16 km and 32 km bsl, where changes in the vertical velocity gradient are observed, together with the Moho and 60 km depth are used as controlling nodes. The changing velocity reduction with depth is achieved by varying the amplitude of velocity reduction on the controlling nodes. The amplitude of velocity reduction at any depth between two controlling nodes is linearly interpolated from controlling nodes. In each test, the width of the LVA remains constant in depth, because also varying the width would introduce too many parameters into the inversion, making it too difficult to assess the results. The range of the percentage of velocity reduction on each controlling node is determined as follows:

At the Moho—High-quality Pg, PmP and Pn arrivals are recorded by OBS26, which was deployed in the transform valley (Supplementary Fig. 7a). The PmP arrivals observed on OBS26 (Supplementary Fig. 7b) demonstrate that the mantle velocity must be larger than the crustal velocity (~6.2 km/s) just above the Moho. In our test, we set the maximum amplitude of velocity reduction just below the Moho to 14%, which limits the minimum mantle velocity to 6.75 km/s. The positive travel time residuals ($\Delta t = t_{pick} - t_{cal}$; Supplementary Fig. 7c) of OBS26 suggest that the mantle velocity reduction should be larger than the 8% obtained from tomography. Resolution tests found that when the amplitude of velocity reduction within the inserted LVA is 8%, an LVA wider than 45 km can produce an 8% velocity anomaly at the Moho after tomography (Supplementary Figs. 4e–g). Based on these observations, we limit the maximum width of the inserted LVA to be 45 km at the Moho, with a minimum percentage of velocity reduction of 8%.

16 km depth—To avoid the possible introduction of a negative vertical mantle velocity gradient within the inserted LVA, we constrain the amplitude of velocity reduction at 16 km depth as between that at the Moho and 32 km depth.

32 km depth—The velocity reduction of the recovered LVA using the OBS data is ~2% at 32 km depth, where the mantle velocity below the Romanche TF is ~7.80 km/s and that beneath the normal crustal segment is ~7.95 km/s at this depth (Fig. 3a). The resolution tests show that if the velocity reduction of the inserted LVA is 8% at this depth, the LVA cannot be narrower than 30 km to obtain a recovered velocity reduction of 2% (Supplementary Fig. 4b). Furthermore, it should not be wider than 50 km, otherwise, the recovered velocity reduction is ~3% at 32 km depth (Supplementary Fig. 4f). When the inserted LVA is 50 km wide, resolution tests show that more than 4% of velocity reduction within the inserted LVA is required to produce ~2% of recovered velocity anomaly at 32 km depth (Supplementary Figs. 5b, c). Based on these observations, we set the width range of the inserted LVA at 32 km depth to 30-50 km, with the amplitude of velocity reduction varying from 4% to 8%.

60 km depth—We assume the amplitude of velocity reduction at 60 km depth shares the same range as that at 32 km depth due to the nearly constant tomographic velocity gradient between 32 km and 60 km depth observed in the tomographic result (Fig. 3b). The width of the LVAs used in tests is constant in depth, so varies between 30 km to 50 km.

Based on the above analysis, we create a suite of models (Synthetic models in Supplementary Fig. 8) by inserting LVAs with different widths and changing velocity reductions in depth (Extended Data Table 1) into model A (Supplementary Fig. 6). We calculate travel times through these synthetic models using the same source-receiver configuration as that used in the tomography of the OBS data. The picking uncertainties of the OBS data are assigned to these modelled travel time datasets, in order to eliminate the influence of picking errors on the estimated width and velocity of the LVA. These synthetic travel time datasets are inverted starting from the same initial model as that used in the tomography of the OBS dataset. After tomography, all these synthetic travel time datasets produce velocity models (Inverted results in Supplementary Fig. 8) showing a similar mantle velocity structure to the tomographic result using the OBS data (Fig. 3a) with a LVA in the mantle beneath the Romanche TF. The differences between the LVA obtained using the OBS dataset (Fig. 3a) and those from the synthetic datasets (Inverted results in Supplementary Fig. 8) are measured by L2-norm

$$J = \|m_{obs} - m_{syn}\|_2^2. \tag{1}$$

To compare the velocity difference between the LVAs, we design two windows to select different regions of the LVAs. Window 1 covers the region between horizontal distance 410 km to 430 km and depth from the Moho to 25 km bsl and is used to constrain the width and mantle velocity at the Moho and at 16 km depth. Window 2 with horizontal distance from 400 km to 440 km and depth from 25 km to 60 km is used to constrain the width and velocity of the LVA at 32 km and 60 km depths. Extended Data Table 1 shows the velocity misfits measured within different windows. We set a misfit threshold to select the synthetic models whose tomographic results have a good fit to the OBS data inverted result. By taking the average of the width and velocity of the introduced LVA in the selected models, we estimate the width and amplitude of velocity reduction of the real LVA below the Romanche TF (Extended Data Table 2). The uncertainties of the width and amplitude of velocity reduction are characterized by their standard deviations. Different misfit thresholds yield very similar estimates (Extended Data Table 2), which validates the stability of our method. In this work, we choose the model parameters obtained using a misfit threshold of 20 (17 models selected for Window 1 and 22 models selected for Window 2 (Extended Data Table 1)) as the final result that is used in the interpretation. Our result shows that the width of the real LVA beneath the Romanche TF varies from 34.1±3.9 km at the Moho to 35.6±5.7 km at 60 km bsl, with the mantle velocity within the LVA being 6.89±0.12, 7.34±0.08, 7.52±0.10 and 7.75±0.06 km/s at the Moho and at 16 km, 32 km and 60 km depths, respectively (Extended Data Table 2).

Finally, we create a synthetic model (hereinafter referred to as 'optimised synthetic model'; Extended Data Fig. 4a) by inserting a LVA with the estimated velocity and width into Model

A (Supplementary Fig. 6). We calculate and then invert travel times calculated using this optimised synthetic model, and the resulting tomographic model (Extended Data Fig. 4b) is compared with that from the OBS data (Fig. 3a). The comparisons give a misfit of 4.5 in Window 1 and 3.8 in Window 2, which demonstrates that the result produced by this inversion is a closer fit to the final OBS data inversion result than the 60 synthetic models listed in Extended Data Table 1. In Supplementary Fig. 9, we compare the travel time residuals for the optimised synthetic model (Extended Data Fig. 4a) and the tomographic model from the OBS data (Fig. 3a). For nearly 85% of all the Pn picks, the optimised synthetic model gives the same or smaller travel time residuals than the tomographic model from the OBS data. Meanwhile, the travel time residuals of ~63% of the Pn picks with rays passing through the transform zone are reduced for the optimised synthetic model. This comparison further demonstrates that the optimised synthetic model has a better fit than the tomographic model from the OBS data.

Temperature and pressure calculation

We use the community software ASPECT version 2.4.0[46] to estimate the temperature of the Romanche transform zone and the neighbouring lithospheric plates following the method proposed in ref. (15). All the parameters and boundary conditions used in the modelling are listed in Supplementary Table 2. The modelling is terminated when a steady state is reached. The brittle weakening of the mantle is modelled using a visco-plastic approximation based on the Drucker Prager frictional plasticity criterion[46]. This setup can produce a similar thermal structure for TF to those described in ref. (37) as suggested in ref. (15), where the warmest temperatures locate at the midpoint of the TF[37] (Supplementary Fig. 10). The effect of deep hydrothermal circulation, which can deepen the thermal isotherms by 1-2 km[36], is not considered in the thermal modelling. The thermal structure along our seismic profile is shown in Fig. 4.

The pressures at different depths are estimated using a model comprising a 5 km-thick water column and a 6 km-thick crust overlying the mantle. The densities of the crust and mantle within the transform zone are set to 2800 kg/m^3 and 3150 kg/m^3, respectively. The estimated pressures at the Moho and at 16 km, 32 km and 60 km depths are 0.21 GPa, 0.37 GPa, 0.86 GPa and 1.73 GPa, respectively.

Serpentinization calculation

We assume the melt-impregnated peridotite[47, 48] is the dominant peridotite within the fault zone, and the olivine-to-serpentine alteration is the dominant reaction in the serpentinization zone. The melt-impregnated peridotite[48] comprises on average 57.6% olivine, 16.5% orthopyroxene, 11.8% clinopyroxene, 1.5% spinel and 11% plagioclase. We assume the anisotropy of the melt-impregnated peridotite is 4%, as a stronger mantle anisotropy is expected within TFs compared to that (~3%) of the normal lithospheric mantle in the Atlantic Ocean[24]. The velocities in ridge-parallel direction of 0% and 100% serpentinized melt-impregnated peridotite at the reference temperature (100°C) and pressure (0.01 GPa) condition are 7.88 km/s and 6.13 km/s, respectively[22]. After the temperature-pressure correction using the toolbox from ref. (22), the estimated 6.89±0.12 km/s and 7.34±0.08

km/s velocities at the Moho and 16 km depth (Fig. 3b) correspond to 55±7% and 25±5% of serpentinization (Extended Data Fig. 5), respectively.

Hydration and mylonitization calculation

Mantle velocity variation for increasing amounts of hydrous phases is estimated using an effective medium analysis[25]. We use the same composition for the melt-impregnated peridotite as for the serpentinization calculations to estimate the degree of hydration at medium temperature (T<750°C). At higher temperatures, the melt-impregnated peridotite[48] comprises 58.8% olivine, 7.45% orthopyroxene, 23.85% clinopyroxene, 1.6% spinel and 8.3% plagioclase. We assume the anisotropy of the melt-impregnated peridotite is 4%. P- and S-wave anisotropies used in the calculations are 27% and 56% for chlorite[49] and are 9.6% and 7.0% for amphibole[16]. The elastic parameters of the melt-impregnated peridotite, chlorite and amphibole at different pressure-temperature conditions are obtained from ref. (22).

Natural sampled medium-temperature mylonites comprise on average of 16% chlorites and 24% amphiboles[16]. In our calculations, we assume the relative amount of chlorite and amphibole formed at medium temperature is 2:3. At 16 km depth where the predicted temperature is 420°C (Fig. 4), a total of 28±6% hydrous minerals are required to account for the low mantle velocity (Extended Data Fig. 6a), which means 70±15% of the lithospheric mantle is mylonitic at this depth (Extended Data Fig. 6c). At 32 km depth where the predicted temperature is 940°C (Fig. 4), 10±7% amphibole within the mantle is required to account for the estimated mantle velocity of 7.52±0.10 km/s (Extended Data Fig. 6b). Natural sampled high-temperature peridotite mylonites comprise 12.5% amphibole on average[16], and this means that   24% of the lithospheric mantle at this depth is mylonitic (Extended Data Fig. 6d).

Excess temperature computation

We calculate the excess temperature required for explaining the velocity reduction between 32 and 60 km depths assuming the velocity reduction within the transform zone is only caused by the temperature variation. A derivative of mantle velocity with respect to temperature[50] of -0.525 m/s/°C is used in the calculation. The velocity decrease within the fault zone (Supplementary Fig. 11a) is obtained by computing the difference between the best estimated mantle velocity of the LVA and the average mantle velocity below the 40 Myr-old lithosphere (Fig. 3b). The excess temperature (Supplementary Fig. 11b) is estimated by dividing the velocity reduction by the mantle velocity derivative with respect to temperature. To explain the velocity reduction below 32 km depth, the temperature of the lithosphere would need to increase by ~690-810°C, making the temperature of the lithosphere higher than 1260°C, which defines the upper boundary of the thermally controlled LAB in the Mid-Atlantic Ocean[12]. However, this high temperature is not possible, because the lithospheric mantle would melt at these temperatures, suggesting that the velocity anomaly below 32 km depth cannot be explained by excess temperature, and some other mechanisms are required to explain the observation.

Melt fraction estimation

Melt fractions between 32 km and 60 km depths are estimated using the effective medium theory[25]. Melt ellipsoids with aspect ratio ranging from 1 to 100 are considered in the estimation. We assume the P-wave velocity in the ridge-parallel direction of the background matrix of mantle is 8.0 km/s. The melt inclusions are assumed to be isolated from each other, and this assumption holds for a low concentration of melt. The density and elastic parameters of melt are taken from ref. (51). In this work, we assume the aspect ratio of melt inclusions is 50, based on the assumption that melt inclusions are in the form of thin film. Therefore, the estimated melt fractions at ~32 km and 60 km depths are 1.30±0.30% and 0.64±0.18% (Extended Data Fig. 7), respectively.

Water content estimation

The serpentine, chlorite and amphibole used in calculations contain 12.3 wt%, 13.0 wt% and 2.2 wt% of water[22], respectively. At the Moho and 16 km depth, the water contents estimated using serpentine only are 6.77±0.86 wt% and 3.08±0.62 wt%, respectively. Using chlorites and amphiboles, the estimated water contents at 16 and 32 km depths are 1.81±0.39 wt% and 0.22±0.15 wt%, respectively. The mismatch of water contents estimated from serpentine and chlorite/amphibole at 16 km depth may result from the use of inaccurate anisotropies and velocities of peridotites and hydrous minerals or the possible co-existence of different hydrous minerals.

The water contents required to enable hydrous melting of mantle between 32 and 60 km depths are estimated using the model and parameters described in ref. (26). Melt fractions of 1.30% and 0.64% are used in the estimation of water contents at 32 and 60 km depths, respectively. Our calculation shows that the required water content is 0.22 wt% at 32 km and no water is required at 60 km depth (Extended Data Fig. 8). This demonstrates that the water content in the mantle between 32 and 60 km depth below the Romanche TF decreases with depth, which is consistent with the water content variation in the LAB[12].

Extended Data
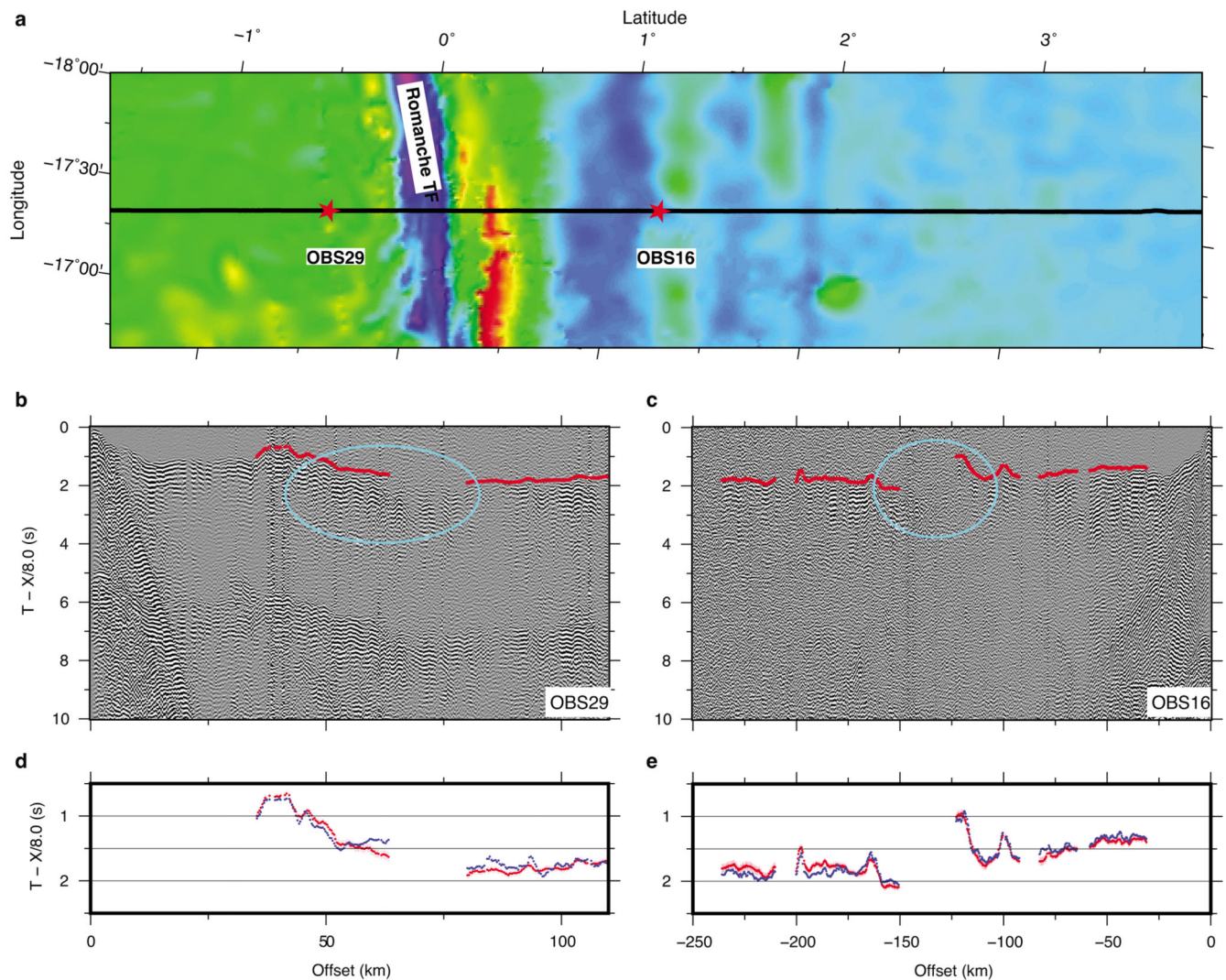
Extended Data Fig. 1. OBS data at intermediate offsets and comparisons of picked and modelled travel times
a, Bathymetry map showing the location of the Romanche TF, the seismic profile (black line) and the locations of OBSs (red stars). **b, c,** Seismic sections and the picked Pn travel times, marked in red. The seismic data are plotted at travel time reduced at a reduction velocity of 8.0 km/s. The effect of bathymetry variations is removed by subtracting the propagating time in water, assuming a water velocity of 1.5 km/s. The cyan ellipses on the seismic plots indicate the location of the Romanche transform zone. A travel time delay and amplitude weakening are observed on the seismic sections where the seismic waves enter the Earth within the Romanche transform zone. **d, e,** Comparisons of picked travel times (in red) and modelled travel times (in blue). The red error bars indicate the picking uncertainty. **b, d** for OBS29 and **c, e** for OBS16. The zero offset corresponds to the OBS location.
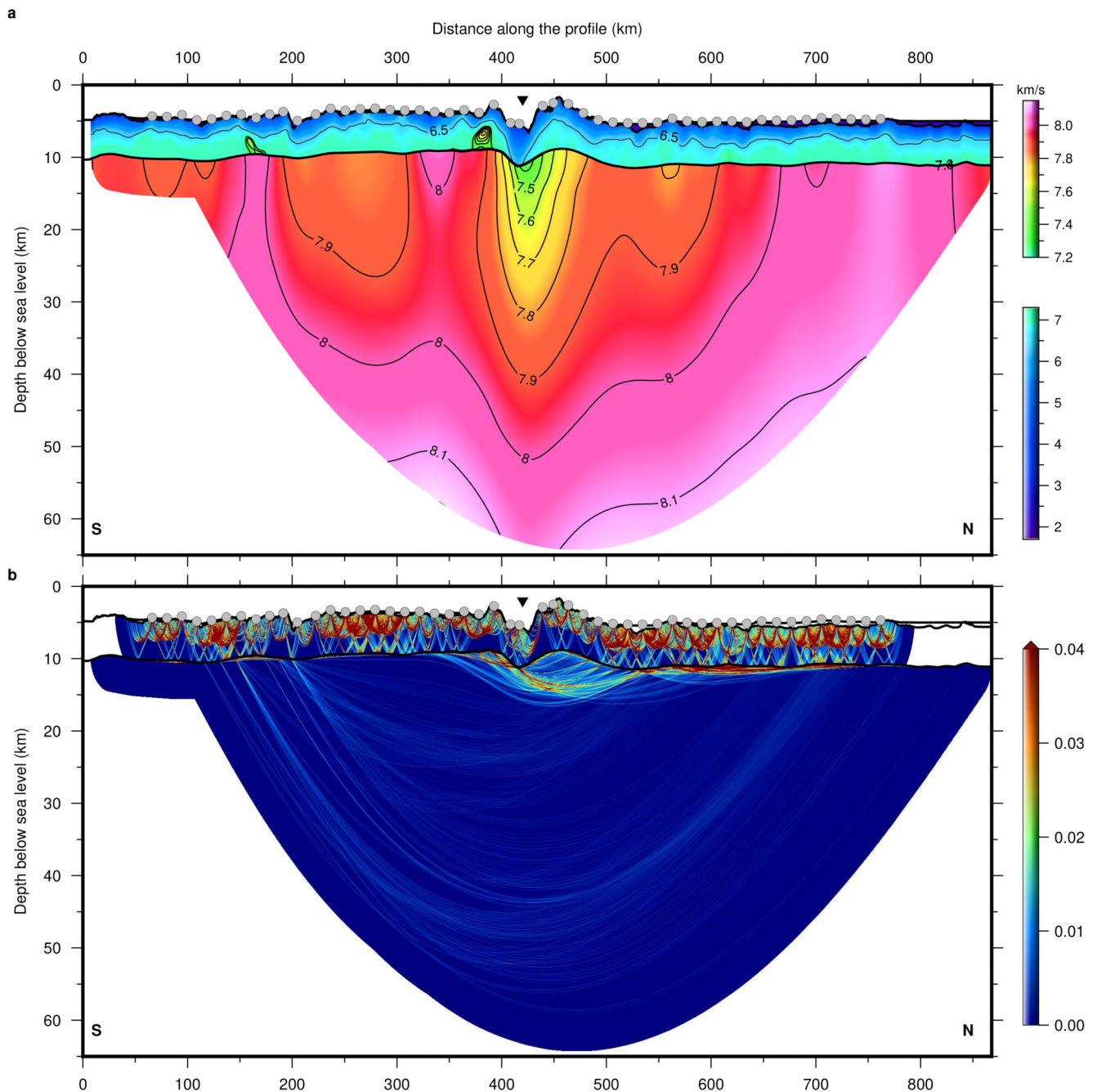
Extended Data Fig. 2. Final tomographic model and the density of ray coverage
a, Final tomographic model and **b**, the density of ray coverage. The black contours and the numbers indicate the velocity in km/s. The maximum ray sampling depth is ~60 km in the final inverted model. The grey circles represent the locations of OBSs. The inverted triangles show the location of the Romanche transform zone. The portion of the tomographic velocity model within 200-650 km profile distance range is shown in Fig. 3a. The zero distance starts from the south along the profile shown in Fig. 1.
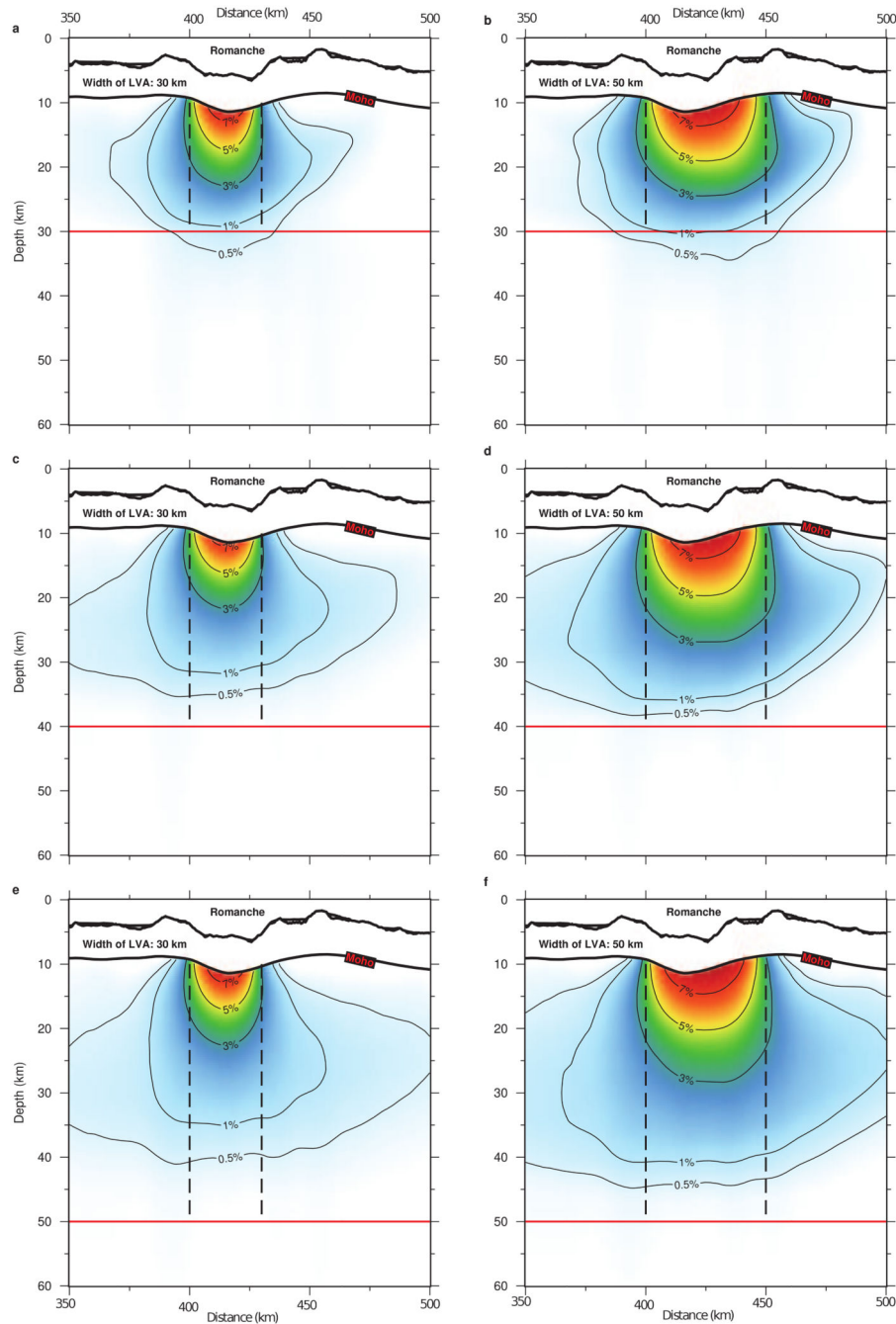
Extended Data Fig. 3. Vertical smearing tests

Smearing effect tests for a low-velocity anomaly (LVA) in the mantle extending down to 30 km (**a** and **b**), 40 km (**c** and **d**) or 50 km (**e** and **f**) depth beneath the Romanche TF. The width of the inserted LVA is 30 km in **a,c,e** and 50 km in **b,d,f**. The black dashed lines represent the side boundaries of the inserted LVAs and the red solid lines show the base of the LVAs. The numbers labelled on the contours represent velocity reduction in percentage after the inversion.
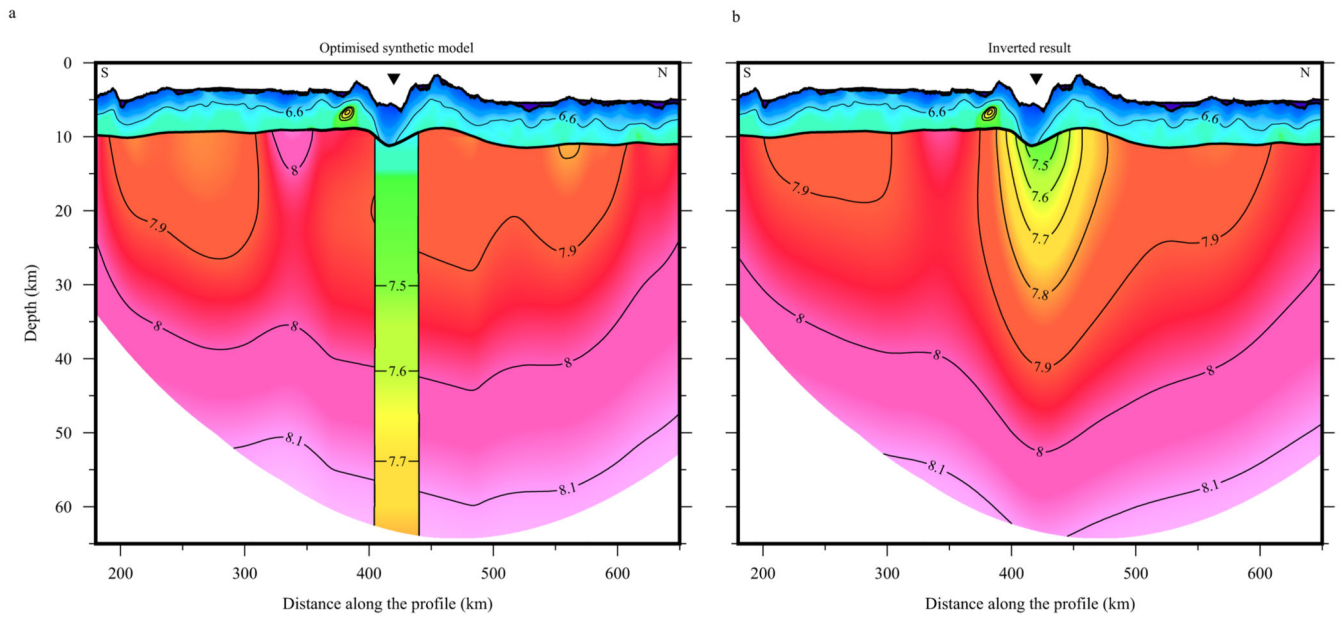
Extended Data Fig. 4. Optimised synthetic mantle velocity model
a, Optimised synthetic mantle velocity structure including a low-velocity anomaly with the final estimated width and velocity (Extended Data Table 2). **b**, Tomographic result of the travel times modelled using the synthetic model in **a**. The inverted black triangles indicate the location of the Romanche transform valley. The black contours and the numbers indicate the velocity in km/s.
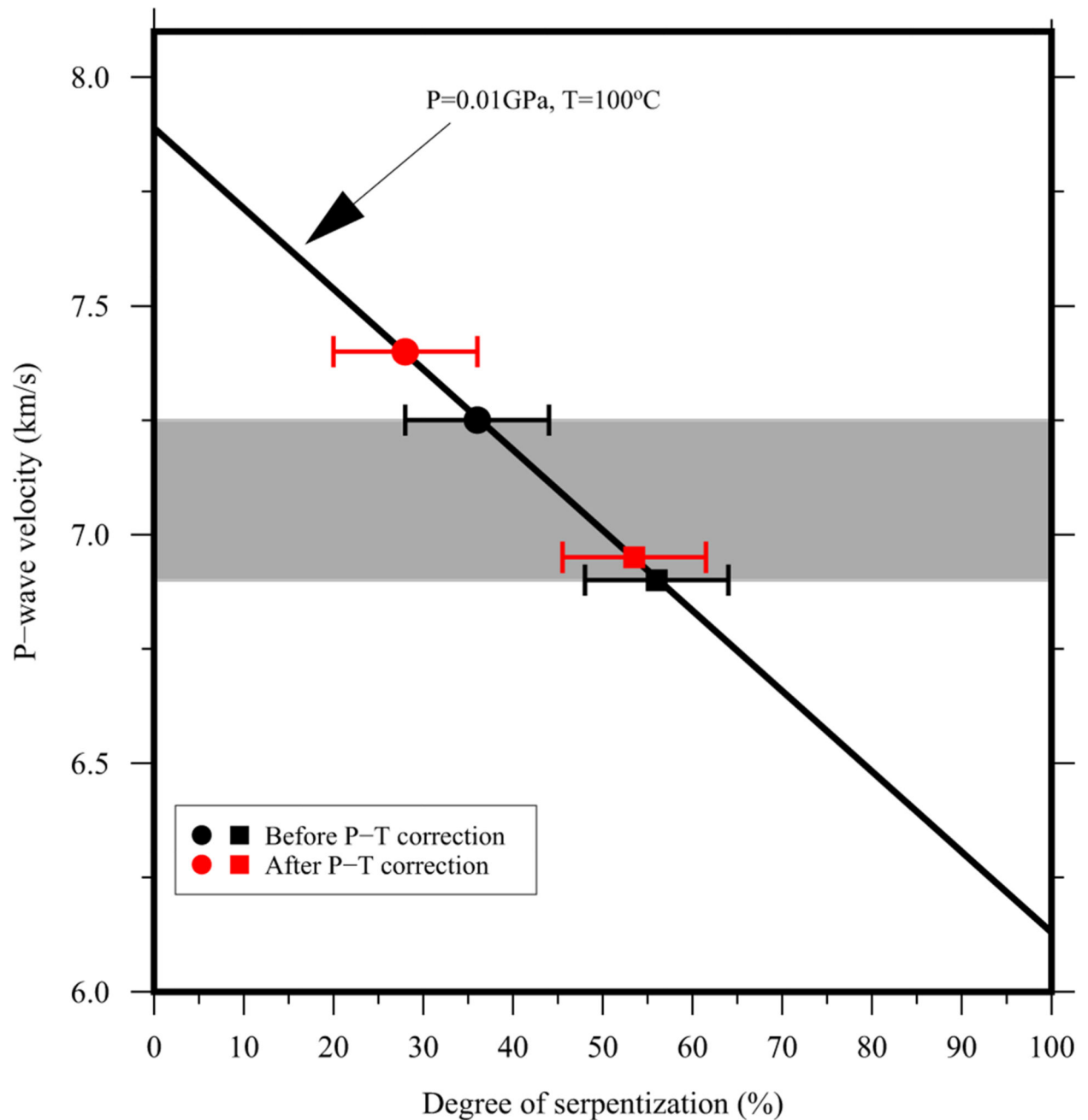
Extended Data Fig. 5. Mantle serpentinization estimate

The mantle P-wave velocity as a function of the degree of mantle serpentinization (black solid line) at pressure P=0.01 GPa and temperature T=100 °C. The grey zone represents the estimated mantle velocity within the Romanche transform zone above 16 km depth. The squares and dots represent the mantle velocities at the Moho and at 16 km depth, respectively, before and after P-T corrections. The bars indicate the uncertainty bounds.
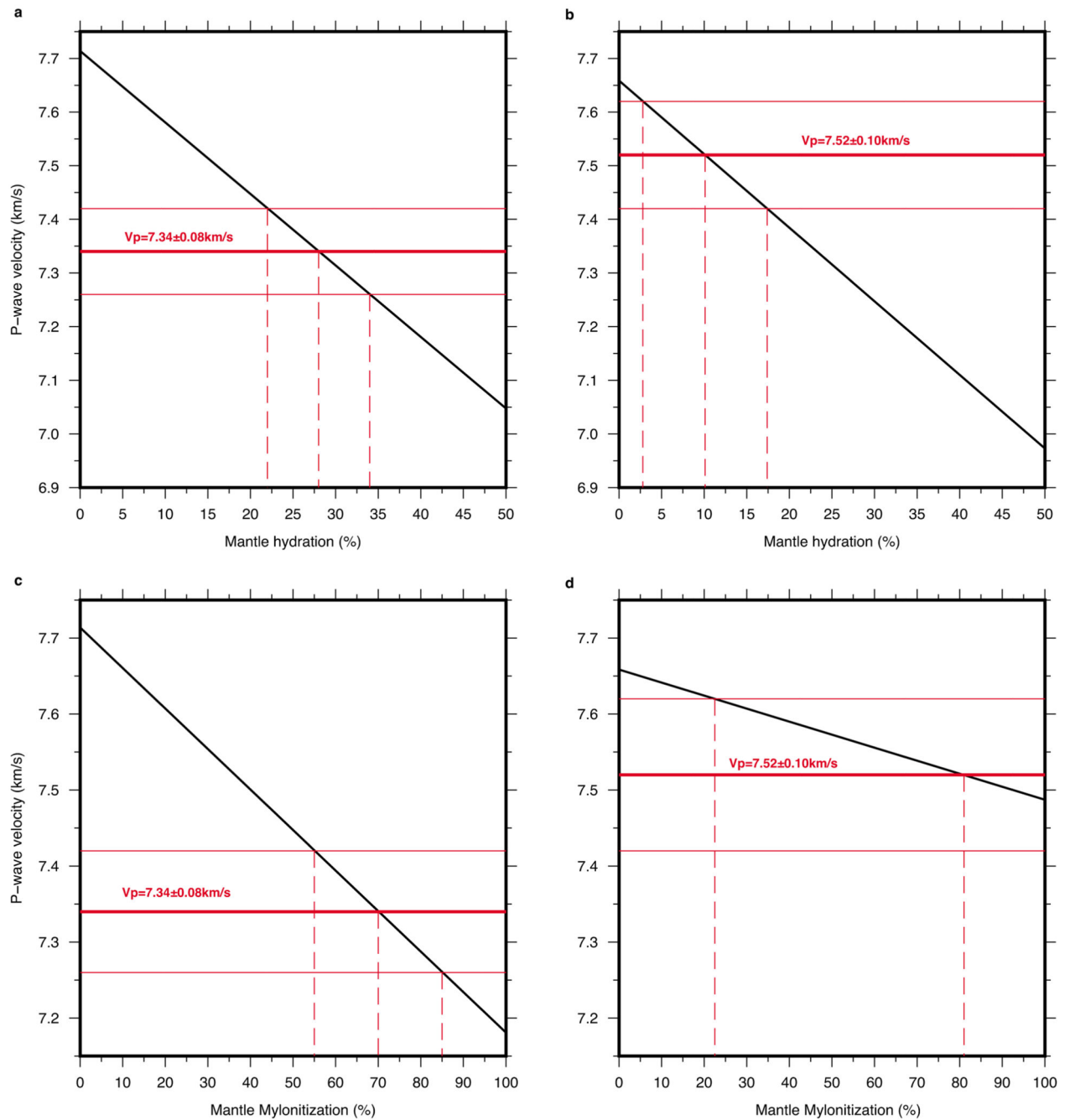
Extended Data Fig. 6. Mantle hydration and mylonitization estimates
The mantle P-wave velocity (black line) as a function of degree of hydration (**a, b**) or degree of mylonitization (**c, d**). **a, c,** for 16 km depth and **b, d,** for 32 km depth. The thick red solid lines indicate the velocities at 16 km and 32 km and thin red lines are uncertainty bounds. The red dashed lines are bounds in %.
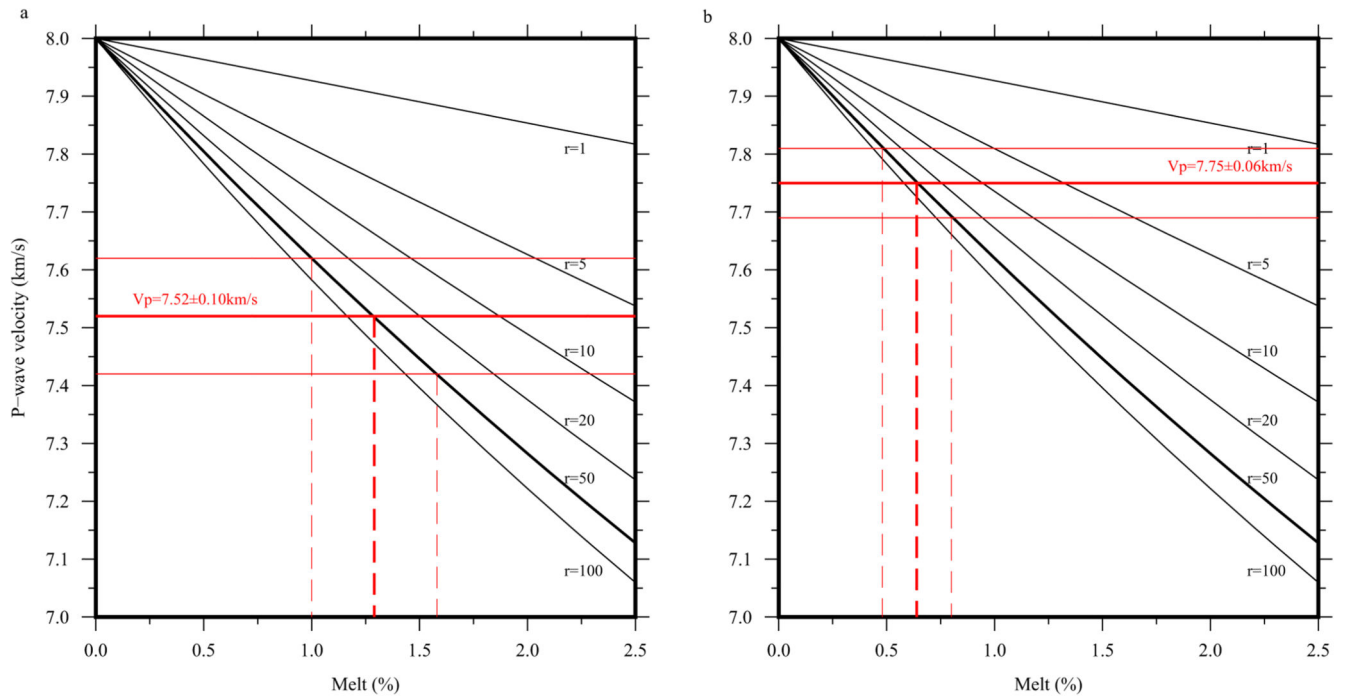
Extended Data Fig. 7. Melt fraction estimation

P-wave velocity variation as a function of melt fraction at 32 km (**a**) and 60 km (**b**) depths below sea level. The aspect ratio of melt r=50 is used in the estimations. The thick red solid lines indicate the velocity at each depth and the thin red lines are uncertainty bounds. The thick red dashed lines indicate the estimated melt fractions, and the thin dashed lines are uncertainty bounds.
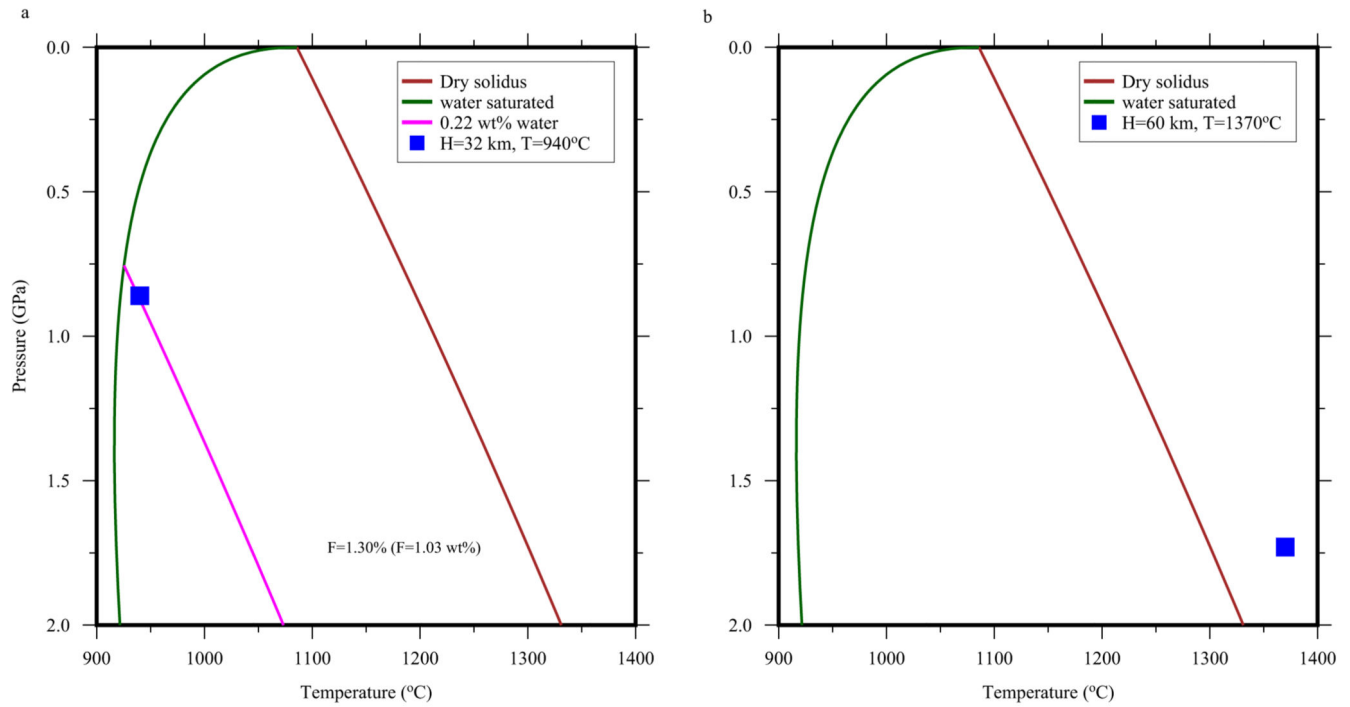
Extended Data Fig. 8. Solidus temperature of mantle
Solidus temperature of mantle with different bulk water content at 32 km depth (**a**) and 60 km depth (**b**).

Extended Data Table 1
Parameters and misfits of synthetic models.

The rows marked in green, blue and red represent the synthetic models that fit the tomographic result using OBS data in Window 1, Window 2 or both, respectively.

Model ID	Width (km)	Velocity reduction at Moho	Velocity reduction at 16 km	Velocity reduction at 32 km	Velocity reduction at 60 km	J in Window 1	J <20	J in Window 2	J <20
1	30	14%	4%	4%	4%	148.6		162.3	
2	30	14%	6%	4%	4%	38.9		80.9	
3	30	14%	6%	6%	4%	15.5		7.6	
4	30	14%	6%	6%	5%	13.3		6.6	
5	30	14%	6%	6%	6%	14.9		6.9	
6	30	14%	8%	4%	4%	12.5		21.5	
7	30	14%	8%	6%	4%	9.4		16.3	
8	30	14%	8%	6%	5%	12.3		11.8	
9	30	14%	8%	6%	6%	27.5		14.6	
10	30	14%	8%	8%	4%	10.4		10.6	
11	30	14%	8%	8%	5%	21.6		15.9	
12	30	14%	8%	8%	6%	34.2		40.8	

Model ID	Width (km)	Velocity reduction at Moho	Velocity reduction at 16 km	Velocity reduction at 32 km	Velocity reduction at 60 km	J in Window 1	J <20	J in Window 2	J <20
13	30	14%	8%	8%	7%	29.0		26.7	
14	30	14%	8%	8%	8%	27.0		48.9	
15	30	14%	10%	4%	4%	96.6		29.7	
16	30	14%	10%	6%	4%	106.9		64.0	
17	30	14%	10%	6%	5%	85.6		70.3	
18	30	14%	10%	6%	6%	111.6		74.5	
19	30	14%	10%	8%	4%	107.5		85.1	
20	30	14%	10%	8%	5%	126.5		77.1	
21	30	14%	10%	8%	6%	130.7		120.6	
22	30	14%	10%	8%	7%	138.5		94.9	
23	30	14%	10%	8%	8%	165.3		169.9	
24	35	12%	4%	4%	4%	32.7		7.9	
25	35	12%	6%	4%	4%	14.5		6.1	
26	35	12%	6%	6%	4%	18.1		6.9	
27	35	12%	6%	6%	5%	18.6		7.8	
28	35	12%	6%	6%	6%	15.6		9.1	
29	35	12%	8%	4%	4%	11.8		5.9	
30	35	12%	8%	6%	4%	11.1		5.2	
31	35	12%	8%	6%	5%	35.4		39.1	
32	35	12%	8%	6%	6%	49.9		55.9	
33	35	12%	8%	8%	4%	20.7		34.6	
34	35	12%	8%	8%	5%	22.7		43.7	
35	35	12%	8%	8%	6%	31.2		59.7	
36	35	12%	8%	8%	7%	33.9		71.6	
37	35	12%	10%	4%	4%	47.7		25.5	
38	35	12%	10%	6%	4%	72.3		65.5	
39	35	12%	10%	6%	5%	65.5		69.0	
40	35	12%	10%	6%	6%	102.6		141.5	
41	40	10%	4%	4%	4%	34.4		12.7	
42	40	10%	6%	4%	4%	14.1		5.2	
43	40	10%	6%	6%	4%	7.6		8.9	
44	40	10%	6%	6%	5%	7.3		12.3	
45	40	10%	6%	6%	6%	7.4		26.1	
46	40	10%	8%	4%	4%	58.1		36.5	
47	40	10%	8%	6%	4%	43.3		46.6	
48	40	10%	8%	6%	5%	60.8		63.6	
49	40	10%	8%	6%	6%	60.0		96.1	
50	45	10%	4%	4%	4%			4.6	

Model ID	Width (km)	Velocity reduction at Moho	Velocity reduction at 16 km	Velocity reduction at 32 km	Velocity reduction at 60 km	*J* in Window 1	*J* <20	*J* in Window 2	*J* <20
51	45	10%	6%	4%	4%			16.4	
52	45	10%	6%	6%	4%			37.1	
53	45	10%	6%	6%	5%			46.3	
54	45	10%	6%	6%	6%			53.9	
55	45	10%	8%	4%	4%			119.0	
56	45	10%	8%	6%	4%			156.3	
57	50	10%	4%	4%	4%			12.8	
58	50	10%	6%	4%	4%			32.0	
59	50	10%	6%	6%	4%			52.5	
60	50	10%	6%	6%	6%			83.5	

Extended Data Table 2

Estimated width and velocity reduction on the controlling nodes using different misfit thresholds. The estimates from *J*<20 are used in the discussion (highlighted in red).

Misfit threshold	Controlling node	Velocity reduction	Width of LVA (km)
J<15	At Moho	12.31±1.73%	34.2±4.3
	16 km depth	6.92±1.00%	
	32 km depth	5.37±1.13%	
	60 km depth	4.53±O.75%	35.8±5.4
J<20	At Moho	12.35±1.57%	34.1±3.9
	16 km depth	6.71±0.96%	
	32 km depth	5.45±1.23%	
	60 km depth	4.50±0.72%	35.6±5.7
J<30	At Moho	12.54±1.53%	33.6±3.8
	16 km depth	7.09±1.00%	
	32 km depth	5.36±1.35%	
	60 km depth	4.60±0.89%	35.6±5.5

Supplementary Material

Refer to Web version on PubMed Central for supplementary material.

Acknowledgements

Data Availability

The high-resolution bathymetry data, the multichannel seismic reflection data and the OBS data from OBS26 to OBS50 are available online (https://doi.pangaea.de/10.1594/PANGAEA.922331) under the condition of acknowledging Marjanovi et al., 2020 (https://doi.org/10.1029/2020JB020275). The OBS data from OBS01 to OBS15 are available online (https://doi.pangaea.de/10.1594/PANGAEA.937195) under the condition of acknowledging Growe et al., 2021 (https://doi.org/10.1029/2021JB022456). The OBS data from OBS16 to OBS25 are available online (Wang, Zhikai; Singh, Satish C (2022): Seismic refraction data from ILAB-SPARC experiment in the equatorial Atlantic Ocean between Romanche Transform Fault and Saint Paul Fracture Zone. PANGAEA, https://doi.org/10.1594/PANGAEA.946565).

Code availability

The tomography code used in this work will be available on request from the corresponding author.

References

1. Wilson JT. A New Class of Faults and their Bearing on Continental Drift. Nature. 1965; 207: 343–347.
2. Bird P. An updated digital model of plate boundaries. Geochem Geophys Geosyst. 2003; 4: 1027.
3. Bird, P, Kagan, YY, Jackson, DD. Plate tectonics and earthquake potential of spreading ridges and oceanic transform faults, in Plate Boundary Zones. Vol. 30. American Geophysical Union; Washington, D.C: 2002. Geodynamics Series
4. Roland E, Lizarralde D, McGuire JJ, Collins JA. Seismic velocity constraints on the material properties that control earthquake behavior at the Quebrada-Discovery-Gofar transform faults, East Pacific Rise. J Geophys Res. 2012; 117 B11102
5. Gregory EPM, Singh SC, Marjanovi M, Wang Z. Serpentinized peridotite versus thick mafic crust at the Romanche oceanic transform fault. Geology. 2021; 49: 1132–1136.
6. GEBCO Compilation Group. GEBCO 2021 Grid. doi: 10.5285/c6612cbe-50b3-0cff-e053-6c86abc09f8f
7. DeMets C, Gordon RG, Argus DF. Geologically current plate motions. Geophys J Int. 2010; 181: 1–80.
8. Abercrombie RE, Ekström G. Earthquake slip on oceanic transform faults. Nature. 2001; 410: 74–77. [PubMed: 11242043]
9. Norris RJ, Toy VG. Continental transforms: A view from the Alpine Fault. J Struct Geol. 2014; 64: 3–31.
10. Müller RD, Sdrolias M, Gaina C, Roest WR. Age, spreading rates, and spreading asymmetry of the world's ocean crust. Geochem Geophys Geosyst. 2008; 9 Q04006
11. Bonatti E, et al. Steady-state creation of crust-free lithosphere at cold spots in mid-ocean ridges. Geology. 2001; 29: 979–982.
12. Mehouachi F, Singh SC. Water-rich sublithospheric melt channel in the equatorial Atlantic Ocean. Nature Geosci. 2018; 11: 65–69.
13. de Melo GWS, et al. Uppermost Mantle Velocity beneath the Mid-Atlantic Ridge and Transform Faults in the Equatorial Atlantic Ocean. Bull Seismol Soc Am. 2021; 111: 1067–1079.

14. Van Avendonk HJA, Shillington DJ, Holbrook WS, Hornbach MJ. Inferring crustal structure in the Aleutian island arc from a sparse wide-angle seismic data set. Geochem Geophys Geosyst. 2004; 5 Q08008

15. Grevemeyer I, Rüpke LH, Morgan JP, Iyer K, Devey CW. Extensional tectonics and two-stage crustal accretion at oceanic transform faults. Nature. 2021; 591: 402–407. [PubMed: 33731945]

16. Prigent C, Warren JM, Kohli AH, Teyssier C. Fracture-mediated deep seawater flow and mantle hydration on oceanic transform faults. Earth Planet Sci Lett. 2020; 532 115988

17. Kohli AH, Warren JM. Evidence for a Deep Hydrologic Cycle on Oceanic Transform Faults. J Geophys Res. 2020; 125 e2019JB017751

18. Kohli A, Wolfson-Schwehr M, Prigent C, Warren JM. Oceanic transform fault seismicity and slip mode influenced by seawater infiltration. Nature Geosci. 2021; 14: 606–611.

19. McKenzie D, Jackson J, Priestley K. Thermal structure of oceanic and continental lithosphere. Earth Planet Sci Lett. 2005; 233: 337–349.

20. Guillot S, Schwartz S, Reynard B, Agard P, Prigent C. Tectonic significance of serpentinites. Tectonophysics. 2015; 646: 1–19.

21. Hicks SP, et al. Back-propagating supershear rupture in the 2016 Mw 7.1 Romanche transform fault earthquake. Nature Geosci. 2020; 13: 647–653.

22. Abers GA, Hacker BR. A MATLAB toolbox and Excel workbook for calculating the densities, seismic wave speeds, and major element composition of minerals and rocks at pressure and temperature. Geochem Geophys Geosyst. 2016; 17: 616–624.

23. Yu Z, et al. Semibrittle seismic deformation in high-temperature mantle mylonite shear zone along the Romanche transform fault. Sci Adv. 2021; 7 eabf3388 [PubMed: 33837085]

24. Lizarralde D, Gaherty JB, Collins JA, Hirth G, Kim SD. Spreading-rate dependence of melt extraction at mid-ocean ridges from mantle seismic refraction data. Nature. 2004; 432: 744–747. [PubMed: 15592410]

25. Taylor MAJ, Singh SC. Composition and microstructure of magma bodies from effective medium theory. Geophys J Int. 2002; 149: 15–21.

26. Katz RF, Spiegelman M, Langmuir CH. A new parameterization of hydrous mantle melting. Geochem Geophys Geosyst. 2003; 4: 1073.

27. Keller T, Katz RF. The Role of Volatiles in Reactive Melt Transport in the Asthenosphere. J Petrol. 2016; 57: 1073–1108.

28. Wang S, Constable S, Rychert CA, Harmon N. A Lithosphere-Asthenosphere Boundary and Partial Melt Estimated Using Marine Magnetotelluric Data at the Central Middle Atlantic Ridge. Geochem Geophys Geosyst. 2020; 21 e2020GC009177

29. Rychert CA, et al. A dynamic lithosphere-asthenosphere boundary near the equatorial Mid-Atlantic Ridge. Earth Planet Sci Lett. 2021; 566 116949

30. Harmon N, et al. Evolution of the Oceanic Lithosphere in the Equatorial Atlantic From Rayleigh Wave Tomography, Evidence for Small-Scale Convection From the PI-LAB Experiment. Geochem Geophys Geosyst. 2020; 21 e2020GC009174

31. Marjanovi M, et al. Seismic Crustal Structure and Morpho-tectonic Features Associated with the Chain Fracture Zone and their Role in the Evolution of the Equatorial Atlantic Region. J Geophys Res. 2020; 125 e2020JB020275

32. Growe K, et al. Seismic structure of the St. Paul Fracture Zone and Late Cretaceous to Mid Eocene oceanic crust in the equatorial Atlantic Ocean near 18°W. J Geophys Res. 2021; 126 e2021JB022456

33. Fox PJ, Gallo DG. A tectonic model for ridge-transform-ridge plate boundaries: Implications for the structure of oceanic lithosphere. Tectonophysics. 1984; 104: 205–242.

34. Hékinian R, Bideau D, Hébert R, Niu Y. Magmatism in the Garrett transform fault (East Pacific Rise near 13° 27' S). J Geophys Res. 1995; 100: 10163–10185.

35. Maia M, et al. Extreme mantle uplift and exhumation along a transpressive transform fault. Nature Geosci. 2016; 9: 619–623.

36. Roland E, Behn MD, Hirth G. Thermal-mechanical behavior of oceanic transform faults: Implications for the spatial distribution of seismicity. Geochem Geophys Geosyst. 2010; 11 Q07001

37. Behn MD, Boettcher MS, Hirth G. Thermal structure of oceanic transform faults. Geology. 2007; 35: 307–310.

38. Le Voyer M, Cottrell E, Kelley KA, Brounce M, Hauri EH. The effect of primary versus secondary processes on the volatile content of MORB glasses: An example from the equatorial Mid-Atlantic Ridge (5°N–3°S). J Geophys Res. 2015; 120: 125–144.

39. Menard HW, Atwater T. Origin of Fracture Zone Topography. Nature. 1969; 222: 1037–1040.

40. ten Brink US, et al. Seismic imaging of deep low-velocity zone beneath the Dead Sea basin and transform fault: Implications for strain localization and crustal rigidity. Geophys Res Lett. 2006; 33 L24314

41. Fuis, GS, , et al. A Comparison Between the Transpressional Plate Boundaries of South Island, New Zealand, and Southern California, USA: The Alpine and San Andreas Fault Systems, in A Continental Plate Boundary: Tectonics at South Island, New Zealand. Vol. 175. American Geophysical Union; Washington, DC: 2007. Geophysical Monograph Series

42. Fichtner A, et al. The deep structure of the North Anatolian Fault Zone. Earth Planet Sci Lett. 2013; 373: 109–117.

43. Bécel A, et al. Moho, crustal architecture and deep deformation under the North Marmara Trough, from the SEISMARMARA Leg 1 offshore–onshore reflection–refraction survey. Tectonophysics. 2009; 467: 1–21.

44. Moser TJ. Shortest path calculation of seismic rays. Geophysics. 1991; 56: 59–67.

45. Korenaga J, et al. Crustal structure of the southeast Greenland margin from joint refraction and reflection seismic tomography. J Geophys Res. 2000; 105: 21591–21614.

46. Bangerth W, Dannberg J, Gassmöller R, Heister T. ASPECT: Advanced Solver for Problems in Earth's ConvecTion. User Manual. 2020.

47. Seyler M, Bonatti E. Regional-scale melt-rock interaction in lherzolitic mantle in the Romanche Fracture Zone (Atlantic Ocean). Earth Planet Sci Lett. 1997; 146: 273–287.

48. Tartarotti P, Susini S, Nimis P, Ottolini L. Melt migration in the upper mantle along the Romanche Fracture Zone (Equatorial Atlantic). Lithos. 2002; 63: 125–149.

49. Mookherjee M, Mainprice D. Unusually large shear wave anisotropy for chlorite in subduction zone settings. Geophys Res Lett. 2014; 41: 1506–1513.

50. Goes S, Govers R, Vacher P. Shallow mantle temperatures under Europe from P and S wave tomography. J Geophys Res. 2000; 105: 11153–11169.

51. Clark AN, Lesher CE, Jacobsen SD, Wang Y. Anomalous density and elastic properties of basalt at high pressure: Reevaluating of the effect of melt fraction on seismic velocity in the Earth's crust and upper mantle. J Geophys Res. 2016; 121: 4232–4248.
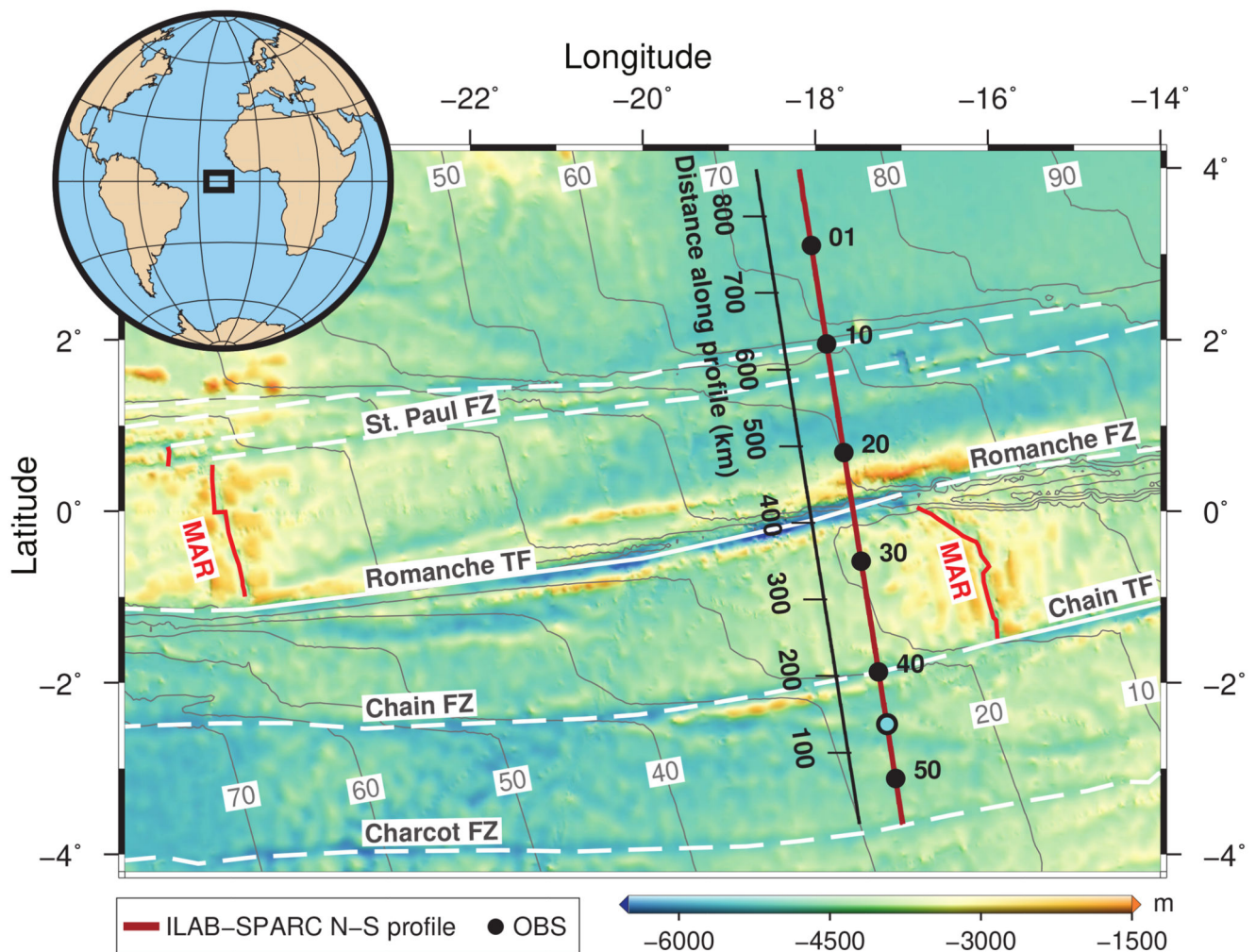
Fig. 1. Bathymetry map of the equatorial Atlantic Ocean.
Bathymetry is plotted by superimposing the high-resolution bathymetry data collected during the ILAB-SPARC experiment on a global low-resolution grid[6] and shows the major TFs (white solid lines) and FZs (white dashed lines). The seismic refraction profile is shown as a brown line, with every tenth OBS location marked by black dots. The cyan dot shows the location of OBS45, which records mantle refraction arrivals up to ~700 km offset shown in Fig. 2. The plate age[10] contours (light grey) are plotted and labelled every 10 Myr. The black scale shows the distance along the profile. The tomographic velocity between 200 and 650 km distances along the profile is presented in Fig. 3a. The black rectangle in the globe inset shows the location of the study area. MAR: Mid-Atlantic Ridge; TF: transform fault; FZ: fracture zone.
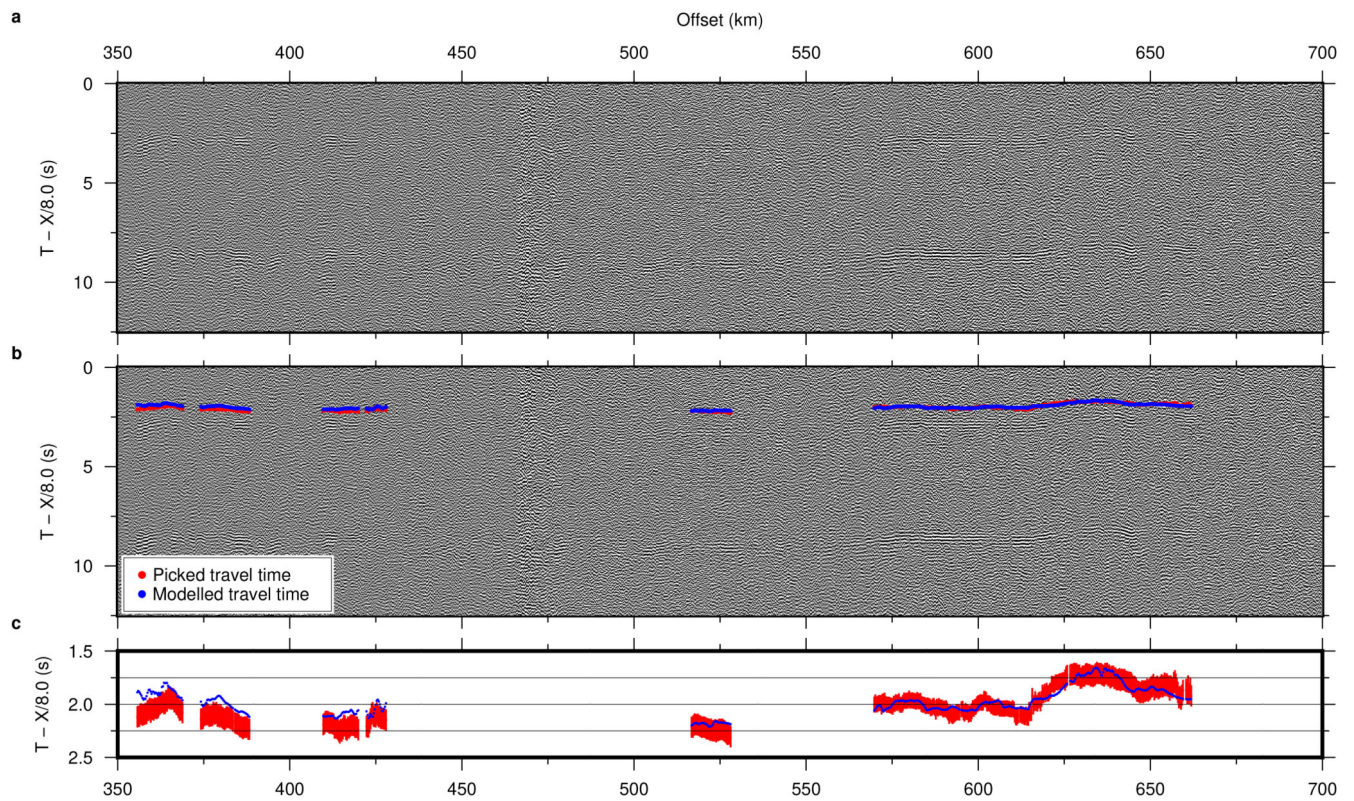
Fig. 2. Ultra-long offset seismic data recorded by OBS45.
a, Pressure data are plotted at the reduced travel time using a reduction velocity of 8.0 km/s. The location of OBS45 is shown by the cyan dot in Fig. 1. The effect of bathymetry variation is removed by subtracting the propagating time in the water, assuming a water velocity of 1.5 km/s. **b,** Same as **a** with picked and modelled travel times of mantle first arrivals. c, Comparison of picked travel times (in red) and modelled travel time (in blue) using tomographic velocity model. The red error bars indicate the picking uncertainty.
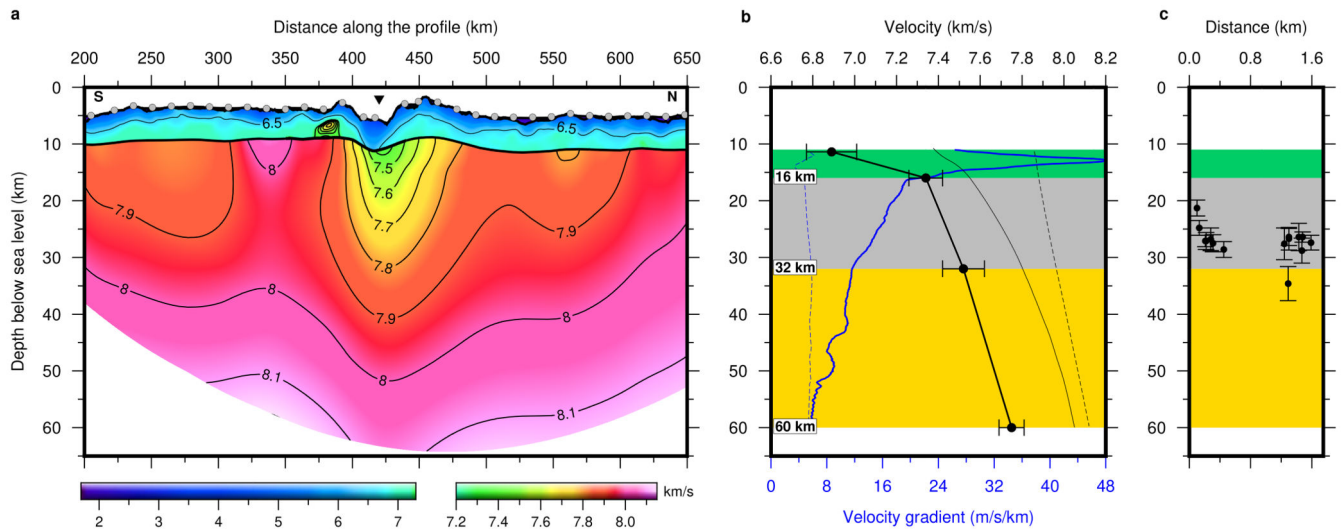
Fig. 3. Velocity structures of the mantle beneath the Romanche transform fault.
a, Tomographic velocity structure obtained from the OBS data. The inverted black triangle indicates the location of the Romanche transform valley. The grey dots show the location of the OBSs. **b,** Solid blue curve shows the average vertical mantle velocity gradient at the centre of the LVA beneath the Romanche TF, at 426-428 km horizontal distance in **a**. The black thin curve shows the average mantle velocity at the centre of the LVA shown in **a** and the black bold curve shows the best simulated mantle velocity of the LVA and their uncertainties (see Methods). The dashed curves show the average velocity (in black) and vertical velocity gradient (in blue) of the normal mantle north of the Romanche TF, at 500-630 km horizontal distance in **a**. Coloured sections indicate the three different zones of lithospheric mantle beneath the Romanche TF, defined by the change in the velocity gradient (see the text). **c,** Focal depth of microearthquakes[22] beneath Romanche TF within 1.6 km horizontal distance to the seismic profile (Supplementary Table 1).
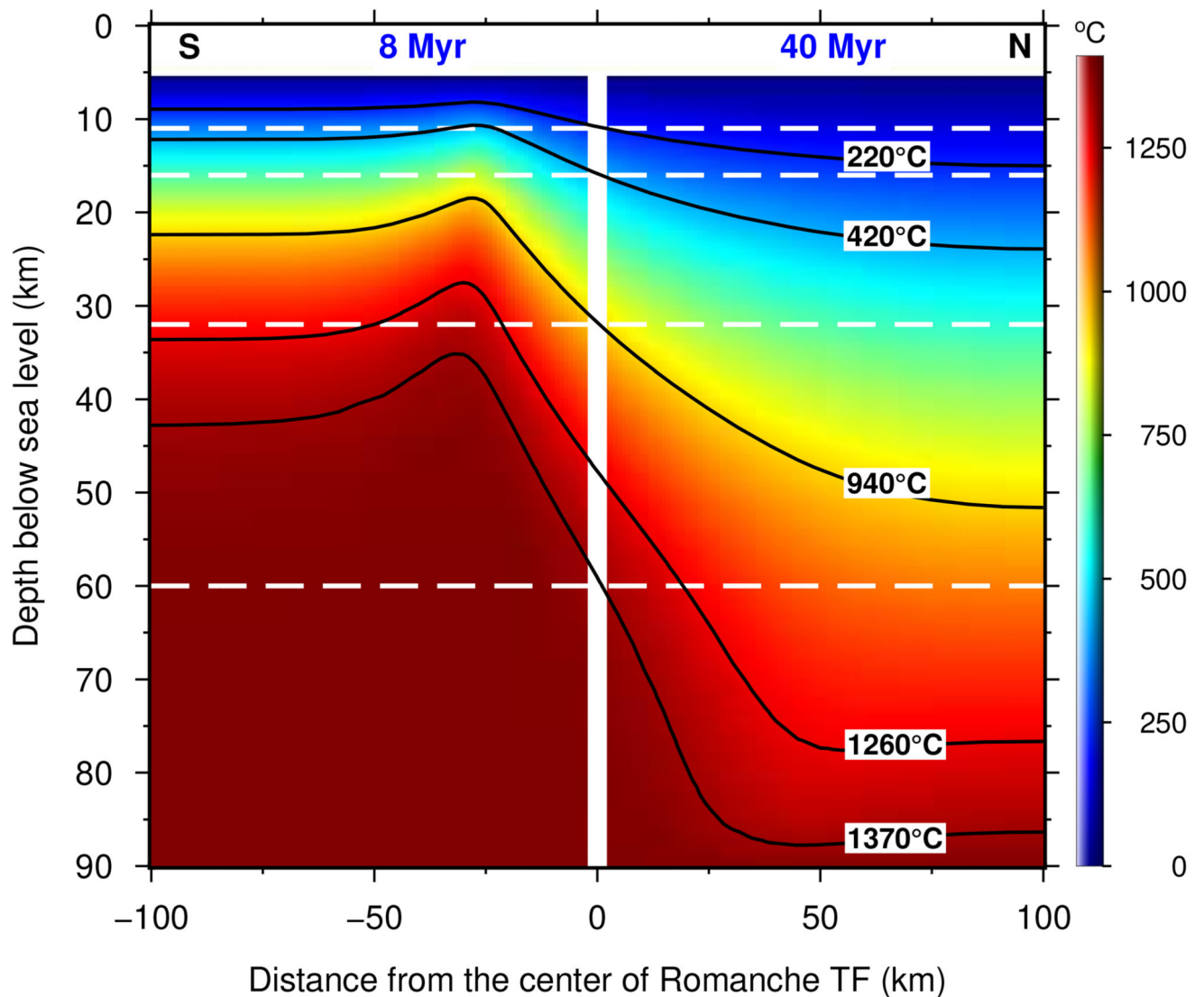
Fig. 4. Thermal structure across the Romanche transform fault along the seismic profile.
The temperature at the centre of the TF is used as the temperature of TF, which is indicated
by the vertical white line. The white dashed lines from top to bottom represent the Moho, 16
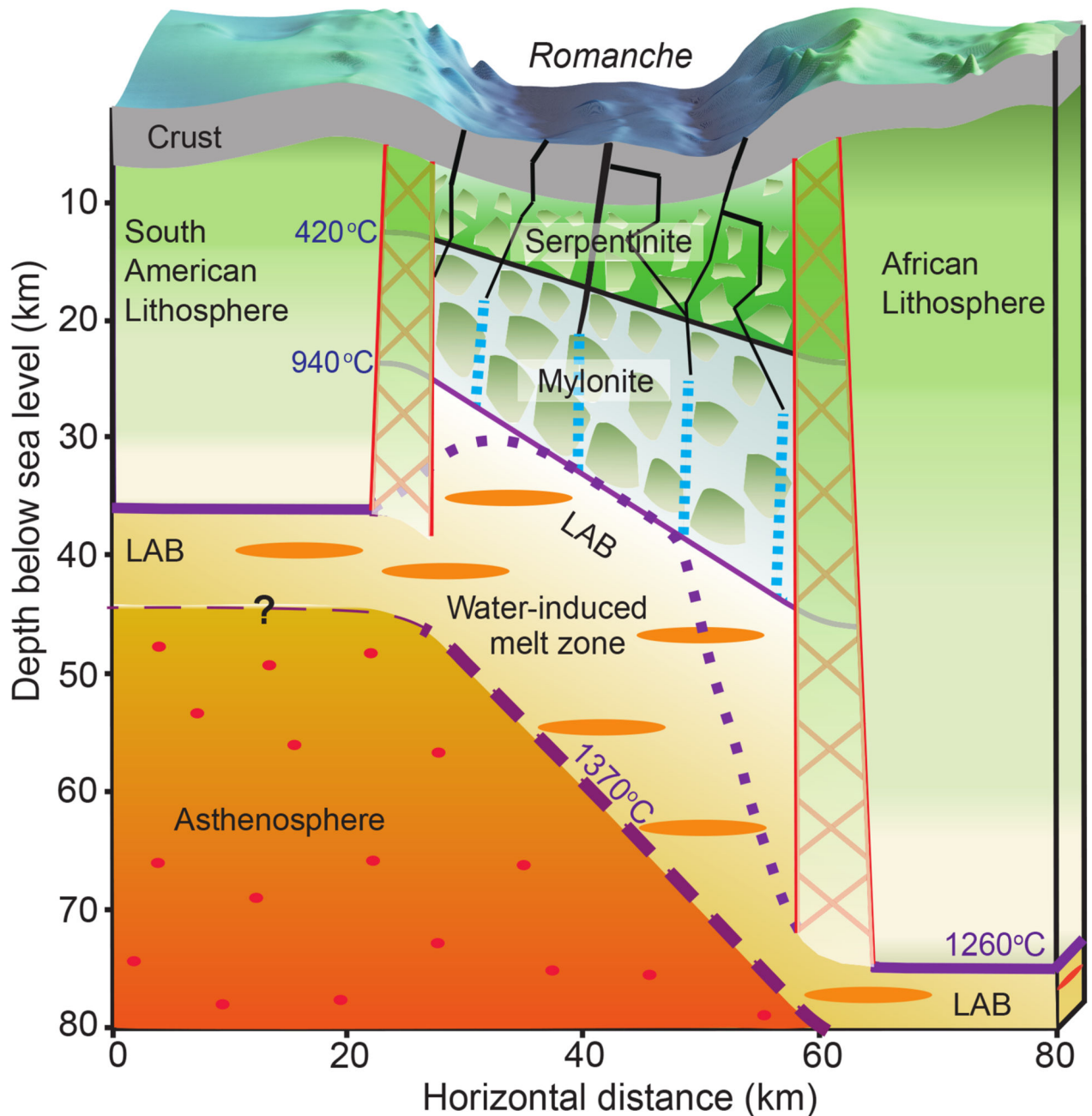km, 32 km and 60 km depths bsl. (See Methods for detailed computation).

Fig. 5. Nature of the lithosphere across the Romanche transform fault.
The 420°C and 940°C isotherms across the Romanche TF are indicated by thin black
and purple lines, respectively, interpreted as the bases of the serpentinized and mylonitic/
hydrous peridotite zones. The blue dashed lines indicate the downward water percolation
promoted by semi-brittle deformation in the mylonite zone. The regions marked by red
crosses represent the transition from the fault zone to the normal oceanic lithosphere. The
thick purple lines mark the 1260°C isotherm for the normal oceanic lithosphere, marking
the LAB[12]. The purple dashed line indicates the 1370°C isotherm defining the bottom of the

sub-lithospheric melt channel at TF. The bottom of the LAB deepens to ~88 km below the 40 Myr-old lithosphere[12], but its depth below the 8 Myr-old lithosphere is not constrained. The interpreted upper boundary of the LAB beneath the Romanche TF (thin purple line) gradually deepens across the TF from the South American plate to the African plate. The purple dotted line is probably closer to the structure of the top of the LAB beneath the Romanche TF.